Initiation and development of tectonic stylolite -Vein system in micritic limestone (Les Matelles, France)

Grégory Ballas, Suzanne Raynaud, Michel Lopez, Emilien Oliot, Jean-Pierre Sizun, Jacinthe Caillaud, Fabrice Barou, Benoit Ildefonse

Initiation and development of tectonic stylolite – Vein system in micritic limestone (Les Matelles, France)

Grégory Ballas [a,*], Suzanne Raynaud [a], Michel Lopez [a], Emilien Oliot [a], Jean-Pierre Sizun [b], Jacinthe Caillaud [c], Fabrice Barou [a], Benoit Ildefonse [a]

[a] Géosciences Montpellier, Université de Montpellier, CNRS, Montpellier, France
[b] UMR 6249, Chrono-environnement, Université de Bourgogne Franche-Comté, Besançon, France
[c] UMR 8187, Laboratoire d'Océanologie et de Géosciences, Université Littoral Côte d'Opale, Wimereux, France

* Corresponding author.
E-mail address: gregory.ballas@umontpellier.fr (G. Ballas).

A B S T R A C T

In this study, we describe the characteristics of tectonic stylolites and related veins affecting a low-porosity micritic limestone (Jurassic carbonates, Les Matelles, South of France) in order to unravel the conditions of initiation and interaction between pressure-solution and fracturing in such rock. Field description, various petrographic and microstructural investigations (cathodoluminescence, *SEM* imaging, *EBSD* analysis), and pet-rophysical/geochemical analyses (*Hg* porosimetry, *XRD, EPMA*) are used. We document that pressure-solution initiates at micropores and propagates along calcite grain contacts, connecting surrounding stylolite micro- segments, and progressively concentrates insoluble material such as clays and siliceous particles. The dis-solved material is evacuated to the veins where the newly-formed porous space is progressively filled by calcite cement. These deformation processes are strictly restricted to the stylolitic interface and veins, as no modification of porosity or grain deformation is detected in the neighboring host rock. This is due to the low-permeability of the surrounding host rock impeding the evacuation of dissolved material and fluids through interstitial porosity around the pressure-solution zone, leading to overpressure and veins formation. The water release and micro-porosity caused by diagenesis of the clay fraction (smectite-illite transformation) are discussed as key diagenetic processes instigating the conditions of pressure-solution initiation, then tectonic stylolite formation in low-porosity limestones.

1. Introduction

Stylolites are described as natural deformation structures formed by dissolution under pressure (pressure-solution) of a soluble host rock or mineral such as calcite or quartz (e.g., Sorby, 1863; Stockdale, 1926; Park and Schot, 1968). These structures are particularly abundant in carbonate rocks where they can form distributed networks (Alvarez et al., 1978; Laronne Ben-Itzhak et al., 2014; Toussaint et al., 2018), or participate to the initiation and the subsequent growth of faults (Peacock and Sanderson, 1995; Willemse et al., 1997; Bussolotto et al., 2015). The study of stylolites bring valuable information in the understanding of diagenesis and burial of rocks (Tada and Siever, 1989; Lavenu et al., 2014; Beaudoin and Lacombe, 2018; Humphrey et al., 2019), the study of paleo stress fields (Arthaud and Mattauer, 1969; Rispoli, 1981; Railsback and Andrews, 1995), or for paleopiezometry (Rolland et al., 2014; Beaudoin et al., 2016). Stylolites and the pressure-solution process were also investigated for their impact on fault rheology (Renard et al., 2000; Gratier et al., 2002), their role on fluid flow systems (Dunnington, 1967; Carozzi and Bergen, 1987; Braithwaite, 1989; Bruna et al., 2018; Beaudoin et al., 2020; Gomez--Rivas et al., 2022), and to evaluate how they affect the petrophysical or mechanical properties of reservoirs (Heap et al., 2014; Baud et al., 2016; Zhou et al., 2022). However, because experimental formation of stylolites represents a technological challenge (Gratier et al., 2005), our knowledge of their initiation and growth, the dynamic of material transfer from solution zones to precipitation zones, and their links with fluids and fracturing remains limited.

Stylolites and veins form in various geological contexts, following different proposed models of initiation and propagation. For diagenetic "sedimentary" stylolite formed during burial, the stress is triggered by the vertical sediment loading, whereas the pore space and the fluids, that are necessary to trigger dissolution and to maintain the dynamics of

material transfer (Dunnington, 1967; Merino et al., 1983), are abundant in the host rock undergoing lithification. In such context, an impact of porosity, clay content or granulometry of the host rock is described on the stylolite occurrence and morphology (Carozzi and Bergen, 1987; Railsback, 1993; Bathurst, 1995; Koehn et al., 2016; Toussaint et al., 2018; Humphrey et al., 2020; Yang et al., 2022). The generation of stylolites can also be triggered by tectonic stress (Arthaud and Mattauer, 1969; Choukroune, 1969; Nenna and Aydin, 2011; Zhou and Aydin, 2012), and are generally considered as structures formed around tension gashes or veins during the initiation and growth of faults (Peacock and Sanderson, 1995; Willemse et al., 1997; Benedicto and Schultz, 2010; Bussolotto et al., 2015). Veins are commonly described as forming first, inducing stylolite formation by local stress disturbance following the crack-anticrack model of Fletcher and Pollard (1981), but also by the pore space and the fluids they supply. However, numerous distributed networks of tectonic stylolites are also described without related fault zones, especially within the Layer Parallel Shortening (LPS) setting (Tavani et al., 2015). In this context, stylolites are associated with related veins showing wedge shape, which indicates that the veins are only secondary structures connected to the firstly formed stylolites (Choukroune, 1969; Nelson, 1981). Since such stylolite networks are described abundantly in low-porosity micritic limestone (Tavani et al., 2010 and references therein), this context raises questions about the conditions of pressure-solution initiation, especially the origin of the fluids that allow the dissolution process, and the pore space that allows the evacuation of the dissolved material.

In the present study, we describe a Jurassic limestone that displays a system of tectonic stylolites and related veins resulting from deformation in the Pyrenean fold-and-thrust belt in the Montpellier area, South of France (Les Matelles village, Petit and Mattauer, 1995). We first provide a detailed description at the macroscopic and microscopic scales of the mineralogical composition and petrophysical properties of the undeformed host rock, in order to document its homogeneity along the sedimentary succession, and to define the diagenetic context of the rock when the stylolite - vein system formed. Stylolites and veins morphology and infilling are analyzed. The relationships between stylolites and veins are described at both the macroscopic and microscopic scales in order to understand their interactions. The impact of such deformation structures on the surrounding rock texture and porosity (i.e., grain shape, size or internal grain deformation) is studied in order to clarify the location and intensity of the pressure-solution and cementation processes, and to discuss the process of material transfer from dissolution to precipitation zones. The results are finally synthetized and used to support a model of tectonic stylolite - vein system development in low-porosity limestone, out of fault zones. The proposed model is then compared to other examples from the literature.

2. Geological setting

The "dalle des Matelles" is a tabular outcrop of gently dipping limestone beds (Upper Kimmeridgian), exposed a few hundred meters northwestward of Les Matelles village (Montpellier area, southeastern France; Fig. 1). This outcrop displays numerous examples of meter-scale deformation structures related to the NS-trending tectonic contraction that has affected this area from the Paleocene to the Upper Eocene (Pyrenean Orogeny, Pic St Loup thrust; Arthaud and Séguret, 1981; Hemelsdaël et al., 2021). Deformation structures are systems of vertical stylolites and veins, organized in pervasive networks and locally disturbed by meter-scale strike-slip faults (Arthaud and Mattauer, 1969; Rispoli, 1981; Petit and Mattauer, 1995; Petit et al., 1999; Soliva et al., 2010; Maerten et al., 2016). A burial depth of a few hundred meters is estimated at the time of deformation, from the thickness of the sedimentary units overlaying the studied section (Late Jurassic – Early Cretaceous). A maximum burial depth of at least 1 km (up to 2 km) was reached before the Albian rifting, and the subsequent erosion of the early cretaceous deposits (Séranne et al., 2002; Barbarand et al., 2020). Bedding-parallel "sedimentary" (diagenetic) stylolites are absent.

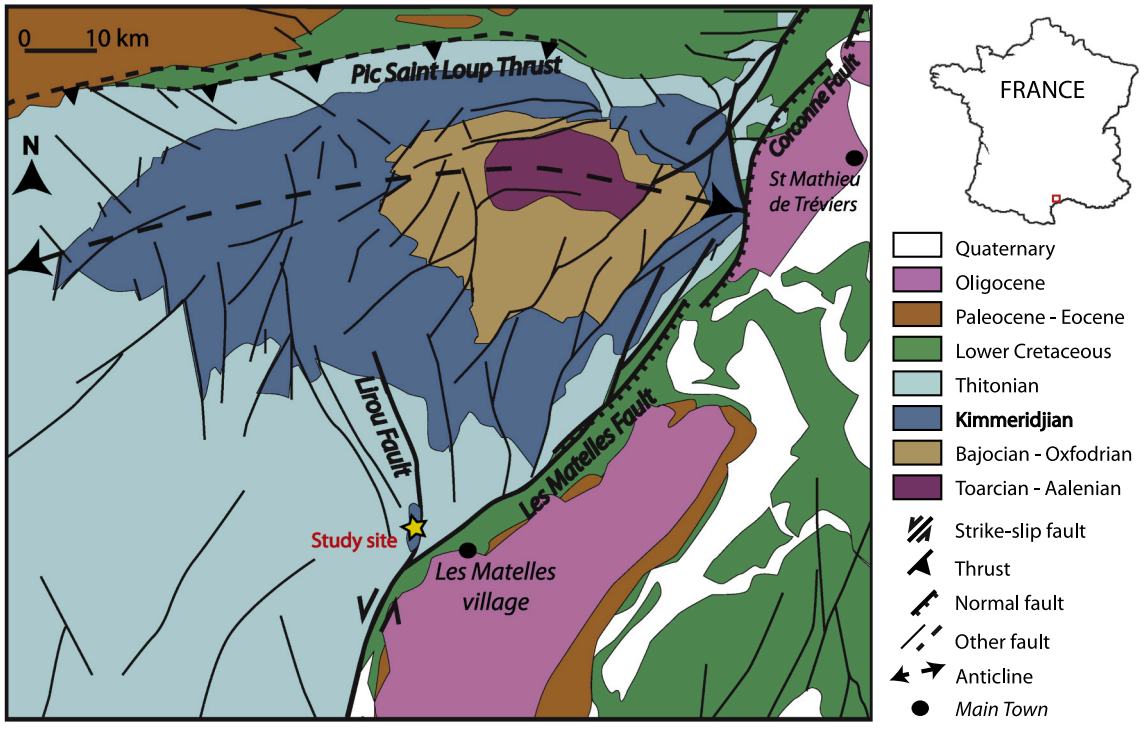

Fig. 1. Geological Map of the study area modified from the Montpellier and St Martin de Londres 1/50 000 geological maps (Andrieux et al., 1972; Philip et al., 1978).

3. Material and methods

3.1. Fieldwork and sampling

A sedimentological log of the studied carbonate succession was done to characterize the host rock and to localize the studied stylolite–vein systems. The strike and dip of stylolites and veins were measured using a tablet (FieldMOVE clino software) and standard compass on each studied carbonate bed. The data are reported on stereographs after restoring the bedding to the horizontal. The organization and morphology of stylolites and veins are described on bed surface in order to clarify their interaction.

We collected 22 host rock samples, one from each exposed limestone bed, in order to characterize the host rock properties along the sedimentary succession (Fig. 2). Additionally, 10 samples were taken in distinct limestone beds to study the stylolites and veins. 14 polished thin–sections were prepared from host rock and stylolite-vein samples for microscopic characterization, and 11 sample parts and mini-cores were used for petrophysical analysis. Two host rock samples were crushed for complementary mineralogical analysis.

3.2. Geochemical analysis

Different geochemical analyses were done to determine the mineralogical composition of the host rock, especially the clay fraction, and to evaluate its homogeneity along the studied section.

An X-ray fluorescence spectrometer (*XRF*, with a Niton® XL3t GOLDD) was used in the field to analyze representative samples from each limestone bed. Each acquired value is an average of 3 measurements per sample. Only values that are 3 times higher than the

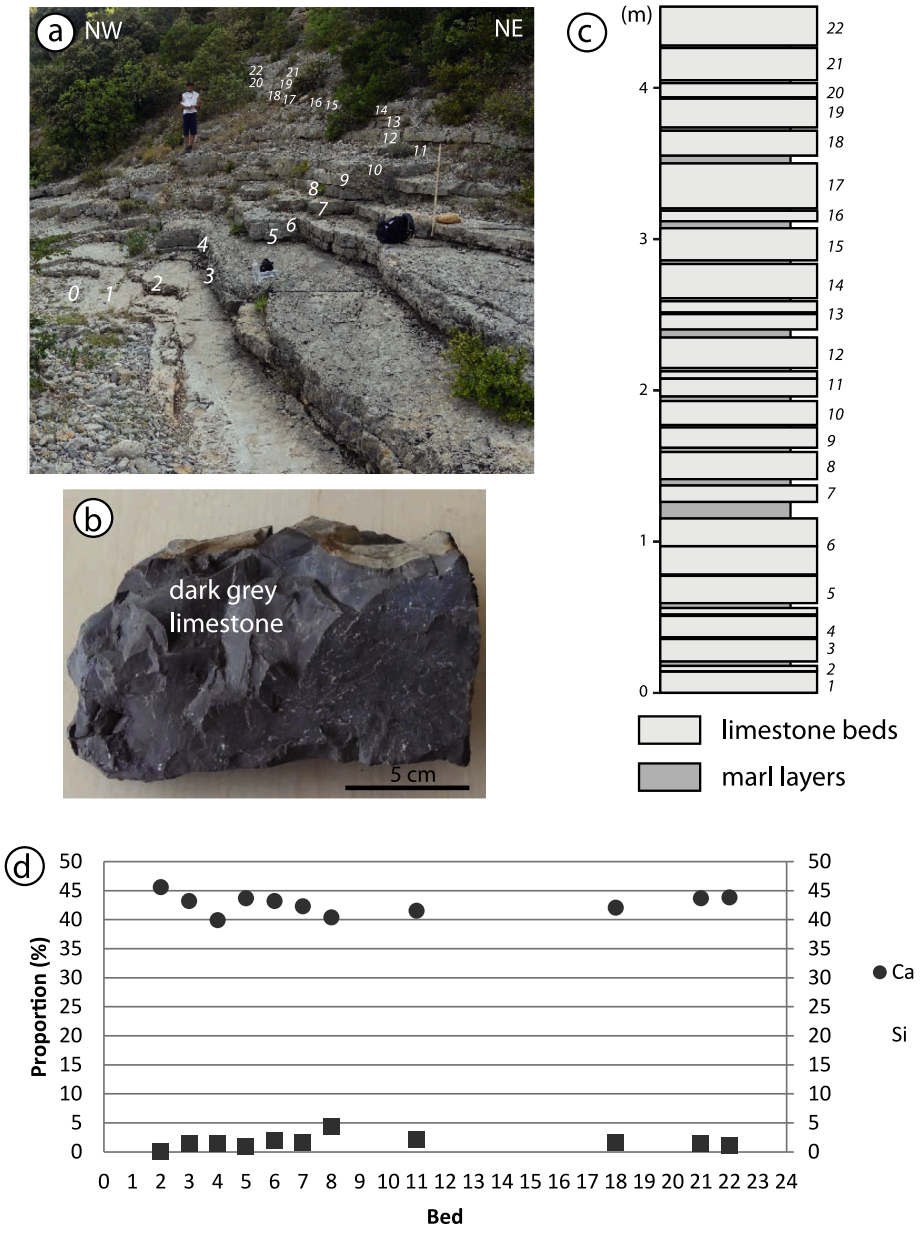

Fig. 2. Stratigraphic succession of Les Matelles outcrop. **(a)** Outcrop of the studied section. **(b)** Limestone sample showing the homogeneity of the rock and its dark grey color. **(c)** Corresponding stratigraphic column. **(d)** Graph showing the proportion of Calcium (Ca) and Silicon (Si) of the different limestone beds of the studied succession (measured by XRF acquisition). Each value is an average of 3 measurements by sample. Only values which are 3 times higher than the measurement error are considered (estimated from the XRF tool). A surface of 6 mm in diameter is analyzed. (For interpretation of the references to color in this figure legend, the reader is referred to the Web version of this article.)

measurement error (given by the XRF tool) are considered. A surface of 6 mm in diameter was analyzed. Clay minerals were identified by X-ray diffraction at the University of Lille, LOG laboratory, using a Bruker AXS D4 Endeavor diffractometer (source: copper) on non-calcareous oriented clay fractions (<2 μm), following to the method described by Bout-Roumazeilles et al. (1999). Clay minerals were identified according to the position of the (001) series of basal reflections on diffractograms (1) air-dried, (2) glycol-coated, and (3) heated to 490 °C (for 2 h). Semi-quantification of clay minerals was carried out on the glycerol curve using the MacDiff software. The reproducibility of technical work and measurements was tested and the relative error is <5%. Then, to determine the type of clay particles along the stylolitic interfaces, Electron Probe Micro-Analyses (*EPMA*) were done on metallized thin-sections using a CAMECA SX-100 electron microprobe (acceleration voltage 15 kV, 4 nA beam current, 1 μm focused beam, Montpellier University, Geosciences Montpellier laboratory). A calculation of structural formulae based on 11O per formula and with the Fe^{3+} state for the iron is used for this determination.

3.3. Microstructures

The microstructures of the host rock and stylolite-vein samples were analyzed using complementary methods.

- optical microscopy in plane-polarized light (*PPL*) mode, cross-polarized light (*CPL*) mode, and cathodoluminescence (*CL*) mode, in order to characterize the rock petrography and the presence of potential cement;
- Scanning Electron Microscopy in backscatter mode (*SEM-BSE*, on a FEI-QUANTA 200 environmental, Montpellier University), in order to precise the pore network properties;
- Electron BackScatter Diffraction (*SEM-EBSD,* on a CamScan Crystal Probe *X*500FE, Montpellier University), in order to quantify the grain characteristics inside and surrounding deformation structures.

Semi-quantitative chemical compositions of grains were also obtained by Energy Dispersive Spectroscopy (*EDS*) punctual analysis and maps acquired during *SEM-BSE* and *SEM-EBSD* analyses.

The grain size, grain shape, and internal grain deformation were quantified from *EBSD* maps acquired across representative examples of stylolites, veins, and undeformed host rocks. Acquisitions were done with a 0.5 μm step size at a working distance of 25 mm. Raw data were first processed using the AZtecHKL software, by removing wild spikes (i.e., isolated misindexed pixel), and filling non-indexed pixels when 7 neighbors with identical orientations were present. The MTEX toolbox for Matlab (e.g., Mainprice et al., 2011) was used to plot crystallographic orientation maps, analyze grain characteristics, and to represent the crystallographic preferred orientations (*CPOs*) using pole figures of the [0001], [1120], [1010] axes (i.e., stereographic diagram, equal area, lower hemisphere, one average orientation per grain is used). The multiple of the uniform distribution (*M.U.D.)* values of these pole figures, and the *J-index* ranging from a value of 1 (random orientation) to infinity (single crystal) (Bunge, 2013; Negrini et al., 2018) were used to determine the *CPO* strength. Grains were reconstructed from the crystallographic orientation data, and their boundaries were defined as having a misorientation angle between neighboring pixels > 10°. The grain orientation spread *(GOS*), which corresponds to the average misorientation of pixels within a grain with respect to the average orientation of the grain, is used to quantify the internal grain deformation.

3.4. Porosity analysis

Two different methods, the mercury injection porosimetry (MIP) and the SEM-BSE image analysis, were combined to characterize the porous network of the host rock, the stylolites, and the veins. These methods provide information on the pore size distribution and connectivity (from MIP), and the porosity location in the host rock and around the deformation structures (from SEM-BSE images).

The MIP method (using a Micromeritics pore-size analyzer Autopore IV, Franche-Comté University) was used to measure the value of the connected porosity on 3D sample and gives detailed information about the distribution of pore access radius (Washburn, 1921; Richard and Sizun, 2011). A total of 11 samples were measured: 7 samples containing deformation structures and 4 samples of the host rocks. The permeability of the host rock was calculated from the porosity and pore access radius using the following law (Purcell, 1949):

$$K = 1.25\ \varphi R^2$$

Where K is the permeability in mD, φ is the porosity in %, and R is the median pore access radius in μm.

The 2D porosity of the host rocks and deformed zones was measured on mosaics of *SEM-BSE* images, with a grey-scale intensity ranging from 0 to 255. The porosity value was obtained considering the black pixels as voids. This method was used along transects crosscutting stylolites and veins in order to analyze the porosity evolution from the undeformed part of the host rock to the stylolites and the veins.

4. Results

4.1. Macroscopic description

4.1.1. Host rock

The Upper Kimmeridgian sedimentary succession of the *La dalle des Matelles* is several tens of meters thick and made of sub horizontal grey-beige limestone beds (Fig. 2a). The beds are regularly stacked with an average thickness of about 20 cm, and shows dark grey break surfaces, suggesting the presence of organic matter and/or clay (Fig. 2b). Mm to cm thick dark clayey-marl layers are generally observed between limestone beds (Fig. 2c). This unit is overlain by the Tithonian unit formed by several meters thick limestone beds and marly-limestone sequences of early Cretaceous age.

4.1.2. Stylolites and veins

Stylolites and veins are generally organized in orthogonal sets pervasively distributed along the bed exposures (Fig. 3). Each stylolite-vein system is affecting a unique limestone bed and is not observed cross-cutting adjacent beds.

Stylolites are observed cutting the bed surfaces as sinuous lines of several tens cm long, and a few mm thick (amplitude between peaks) (Fig. 3a, red color). They are mainly vertical and parallel to each other, striking from N50°E to N70°E (Fig. 3b). The stylolite amplitude, i.e., the distance between opposite peaks, is larger in the central parts of the stylolites (in the horizontal extension, up to 4 mm), and decreases towards their tips. Numerous connections and branching zones are observed between neighboring stylolites, especially when their length exceeds 1 m. Their density is variable from one bed to another and ranges from 6 to 12 stylolites per m.

Veins are also observed on bed surfaces as white or orange regular lines, or almond-shape tension gashes, infilled by calcite cement (Fig. 3a–c, d, blue color). They are vertical, and mainly strike from N160°E to N10°E (Fig. 3b). Veins are generally a few cm to 10 cm long, and their thickness is up to 2 cm, with a large majority of them being a few mm thick. Their spatial distribution is more heterogeneous than that of stylolites. Few examples of en-echelon vein pattern are also observed but are not described in detail since these veins are related to fault zone initiation that is out of the scope of the present study.

The geometry of stylolites is not significantly affected by the presence of veins; only an increase of stylolitic peak amplitude is sometimes observed close to the vein contact. Stylolites bounded by two veins are also locally observed. Conversely, the vein geometry is generally

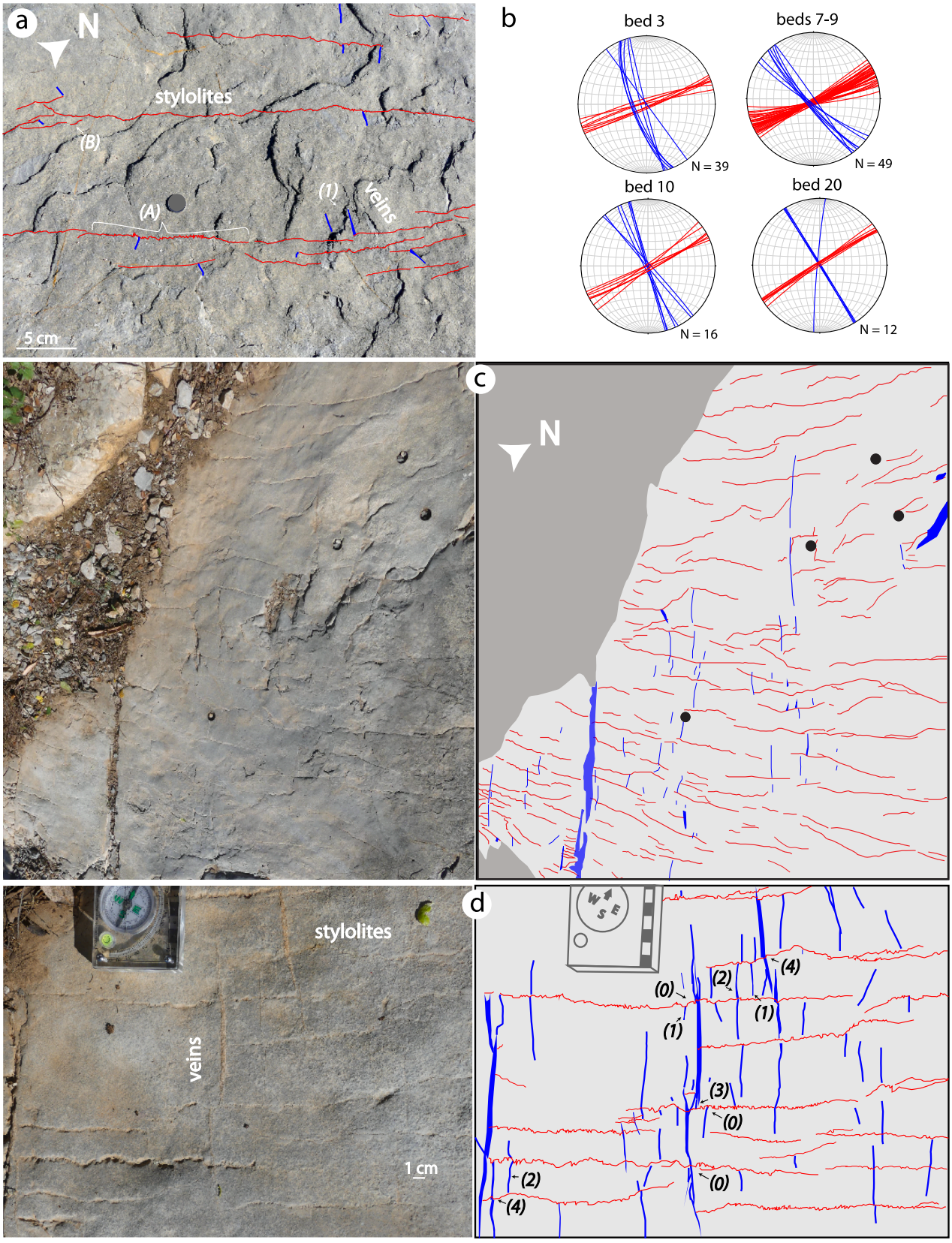

Fig. 3. Macroscopic relationship between stylolites and veins. **(a)** Interpreted photography of the stylolite – vein system observed along a bed surface. **(b)** Stereographic projections showing the orientation of stylolites and related veins in different limestone beds. **(c)** Photography (left) and related interpretation (right) of the dominant stylolite – vein pattern. **(d)** Photography (left) and related interpretation (right) of the detailed interactions between stylolites and veins, respectively. (red: stylolites; blue: veins). (For interpretation of the references to color in this figure legend, the reader is referred to the Web version of this article.)

influenced by the presence of stylolites with different modes of connection and crosscutting relationships (Fig. 3d).

- (1) Vein branched to a stylolite and showing an increase of thickness close to the stylolite (*wing-crack morphology*);
- (2) Veins constrained by two neighboring stylolites and connecting them;
- (3) Vein ramifications, from a unique cm-thick vein to multi small mm-thick veins at the contact with the stylolite;
- (4) Veins crosscut by stylolite with an apparent shear displacement of a few mm.

4.2. Microscopic characteristics

4.2.1. Host rock

The studied host rock, is a micrite with grain sizes of a few microns, as observed from *SEM-BSE* images (Fig. 4a), and an average grain diameter of 2 ± 1 μm calculated from *EBSD* data. The *XRD* analysis confirms that the rock is mainly composed of calcite grains. A small proportion of siliceous particles and clays (Fig. 4a), generally lower than 2%, is detected from the *XRF* data (see the detailed proportions of Ca and Si in the different limestone beds of the studied succession in Fig. 2d). *SEM-BSE* images display a mosaic texture of micritic particles and disseminated μm-size pores between the micro-crystals of calcite (Fig. 4a).

Some fragments of non-identified pelagic micro-organisms and white grains of tens μm size were observed from *PPL* mode microscopy (Fig. 4b–c). The white grains correspond to microsparitic calcite aggregates with an ovoid or rectangular shape that represents pseudomorphs after gypsum or anhydrite micro-crystals, subsequently dissolved during burial. They display the same grey color in *SEM-BSE* images and the same orange cathodoluminescence light than the surrounding micritic matrix (Fig. 4c). These aggregates also include residual micritic mud and iron oxides (hematite, goethite) that result from possible oxidation of pyrite (Fig. 4c). Siliceous particles disseminated in the micrite were identified as both detrital quartz grains and chalcedony

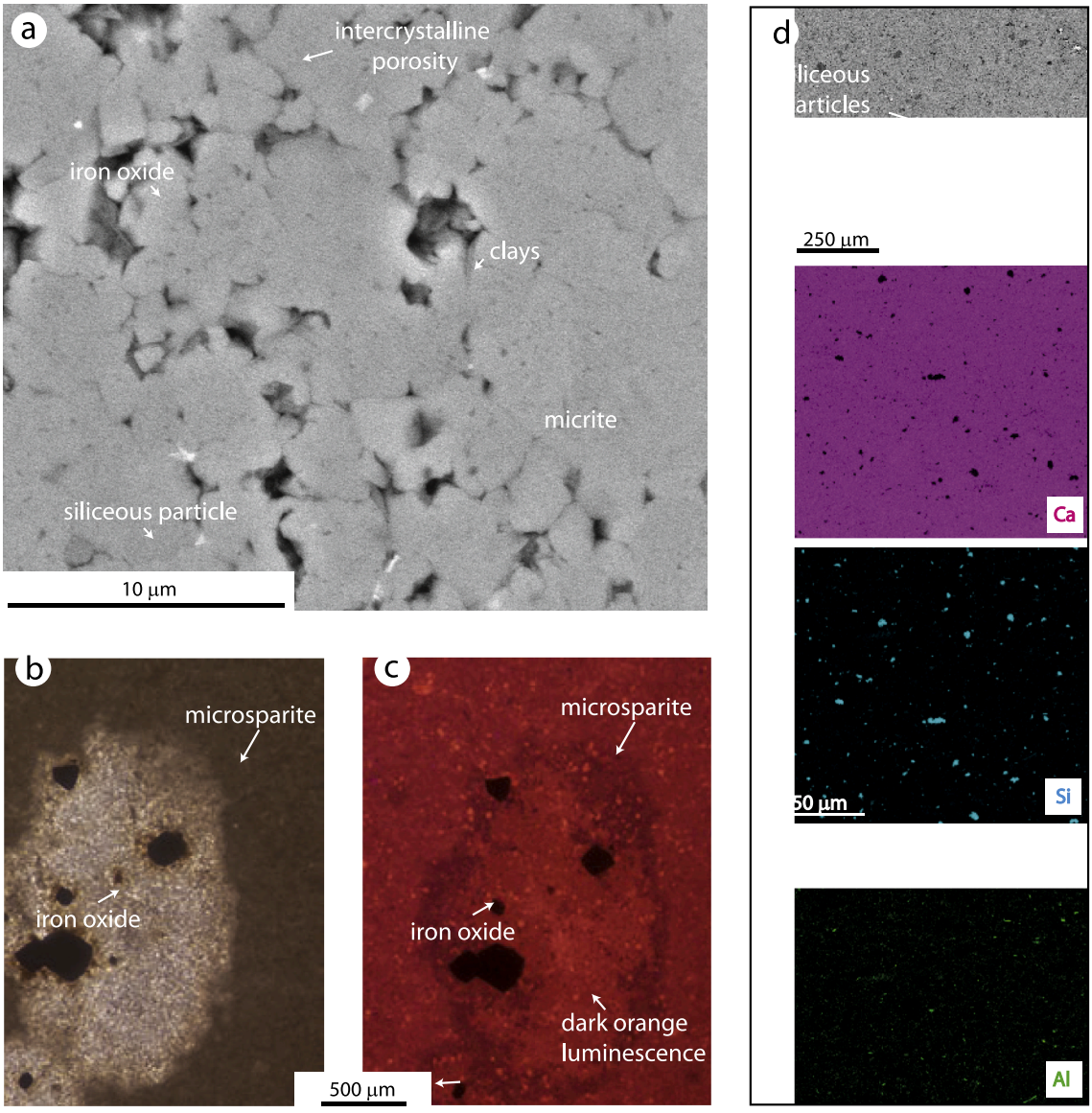

Fig. 4. Microtexture of Les Matelles limestone. **(a)** *SEM-BSE* image of the studied rock. The micritic matrix is dominated by subhedral calcite microcrystals (light grey color), with dispersed siliceous silt-size grains (medium grey color), scarce iron oxides (white), and dark grey clays minerals in the intercrystalline porosity. **(b) (c)** Images of microsparite aggregate including iron oxide, *PPL* and *CL* microscopy respectively. **(d)** *SEM-BSE* image and corresponding *SEM-EDS* map showing the location of calcium (pink), silicon (blue), and aluminum (green). (For interpretation of the references to color in this figure legend, the reader is referred to the Web version of this article.)

diagenetic replacement (Fig. 4a). Low proportions of aluminum, potassium and iron reveal the presence of clay particles disseminated in the pore space (black areas from *SEM-BSE* images) between calcite grains (Fig. 4a–d). The clay minerals were also observed in *SEM* images as elongated particles in their crystallization sites (Fig. 4a). The clay fraction determined by *XRD* analysis is composed of 62% illite, 34% mixed-layer illite-smectite, 3% kaolinite, and <1% chlorite. The granulometry, porosity and mineralogical properties are homogeneous over the whole sedimentary succession.

4.2.2. *Stylolites microstructures*

Stylolites are detected from their brown color that contrasts with the dark grey color of the host micritic calcite (*PPL* mode) (Fig. 5a). This brown color is related to the presence of clay minerals, and is sometimes associated to iron oxides located along the stylolitic suture. The presence of microsparitic calcite aggregates affected by stylolites suggests that deformation occurred after the aggregate formation (Fig. 5a). The stylolite morphology is characterized by peaks with variable wave lengths of amplitude, from a few tens microns to several millimeters (Fig. 5b).

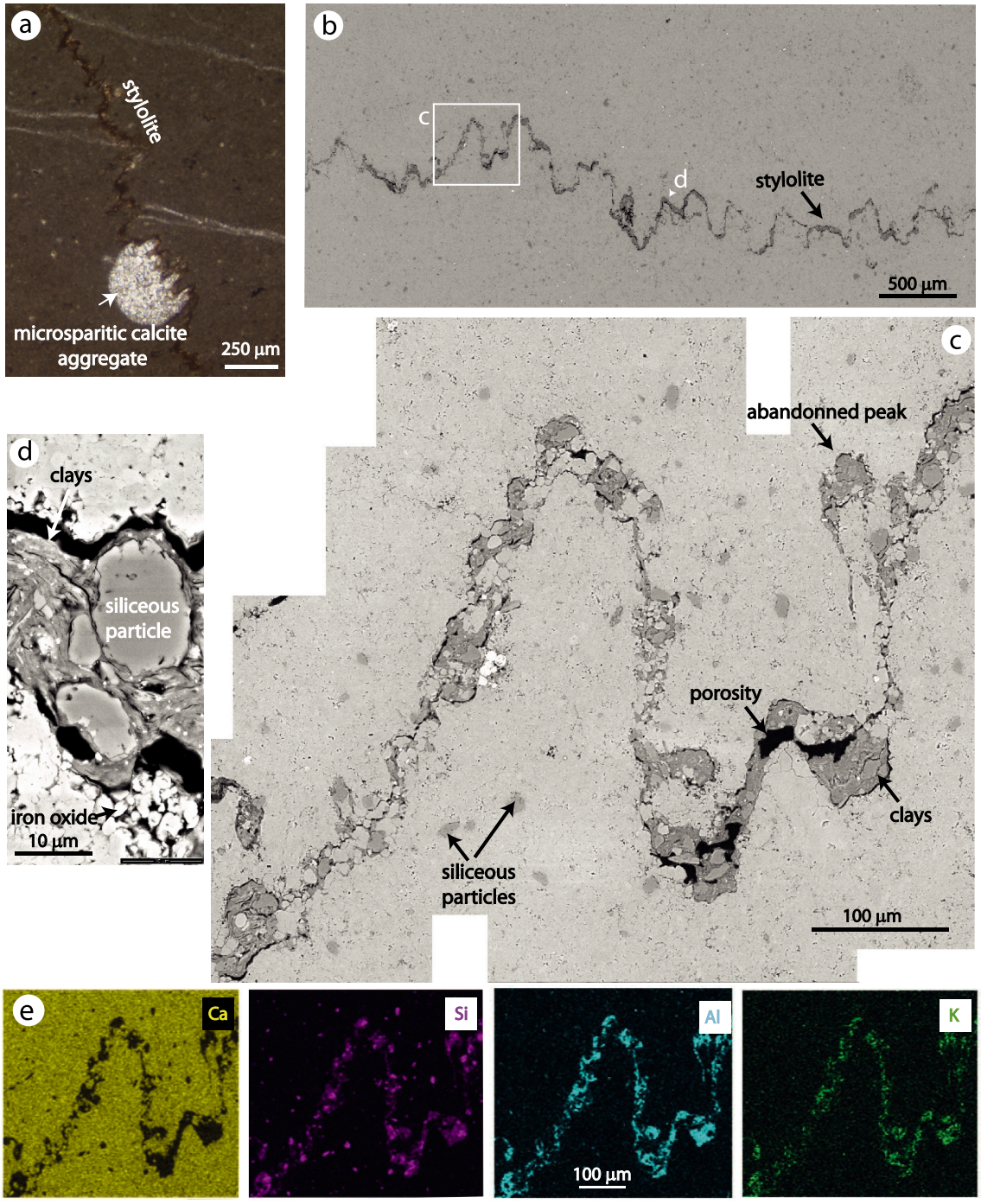

Fig. 5. Microstructure of stylolites. **(a)** *PPL* microscopic image of a stylolite affecting an aggregate of microsparitic calcite. **(b)** Mosaic of *SEM-BSE* images showing the general morphology of stylolite. **(c)** Detailed mosaic of *SEM-BSE* image showing the stylolite peaks and infilling. **(d)** Detail *SEM* image showing the clays and siliceous particles packed within the stylolite interface. **(e)** *EDS* maps showing the concentration of Calcium (Yellow), Silicon (Pink), Aluminum (Blue), and Potassium (Green). Note that the *EDS* maps were acquired for the same zone than the *SEM-BSE* image (c). (For interpretation of the references to color in this figure legend, the reader is referred to the Web version of this article.)

Disconnected peaks along some stylolites are considered as abandoned segments (Fig. 5c). Clays, siliceous particles, and less soluble calcite grains are observed within stylolites in *SEM-BSE* images (Fig. 5c and d). This insoluble material can reach a thickness of several tens of μm, especially at stylolitic peaks. The oblique segments connecting peaks are also filled by insoluble material but their thickness is generally only a few μm. The *EDS* data clearly show the concentration of silicon, aluminum and potassium related to clay and quartz grains concentrations in the stylolite (Fig. 5e), with discontinuous black zones representing void space along the suture (Fig. 5c and d). *EPMA* data show that clay minerals are characterized by tetrahedral charge bearing minerals such as illite (charge 0.8–0.9), and mixed-layer illite-smectite (*I–S*, charge 0.2–0.8) (Fig. 6a), also revealed by *XRD* results on host rock.

We observed the presence of μm-thick structures developed along the calcite grain contacts, and connecting, over several tens μm, porous areas partly infilled by clay minerals and siliceous particles (Fig. 6b and c). These structures have an irregular morphology with peaks, closely similar to the morphology of macroscopic stylolites. These structures are open and porous spaces developed between calcite grains, with no infilling material. They are specifically located at mature stylolite tips or between connected stylolites. These structures form segments several hundred μm long, almost parallel to the mature stylolites, and connected to each other by oblique surfaces. They are considered as zones of incipient pressure-solution and are sometimes observed integrated within the stylolite tips.

4.2.3. *Veins microstructures*

Veins crosscut micro-sparitic calcite aggregates containing iron oxides. Hence, they occurred after the aggregate formation (Fig. 7a). Calcite crystals of different sizes are observed infilling the veins, from micritic (<20 μm) to sparitic calcite crystals (>20 μm). The size and arrangement of calcite crystals depend on the vein thickness:

In narrow veins (narrower than 20 μm), the cement is made of micritic calcite crystals larger than the micritic host rock matrix (Fig. 7b). These veins are detected in *SEM-BSE* images by their different texture related to a porosity lower than in the microporous matrix (Fig. 7b). The calcite crystals are joined and show a blocky morphology that totally fills the pore space, with the exception of a few central vuggy pores (Fig. 7b). These veins also display an orange cathodoluminescence color similar to the microsparitic calcite aggregates, and slightly shinier than the matrix (Fig. 7c). No microcracks are observed in calcite grains next to the veins, which appear to have propagated along the grain contacts. The vein walls are well defined in *CPL* microscopy and appear diffuse in *SEM-BSE* images without any color difference with the host

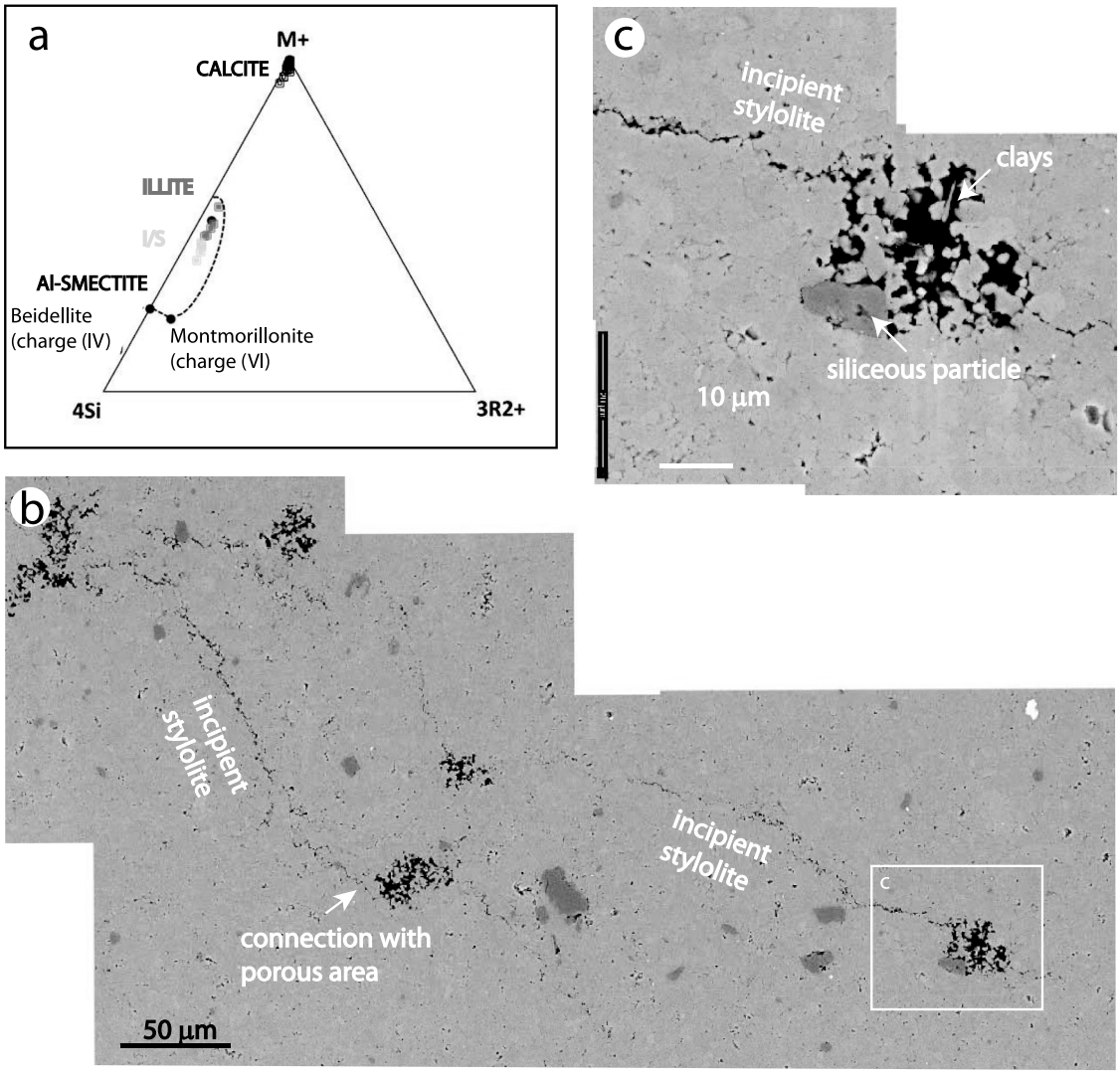

Fig. 6. **(a)** Projection in the M+ 4Si 3R2+ ternary system (Meunier and Velde, 1989) to graphically represent the *EPMA* analyzes of clay minerals infilling pores and stylolites (N = 13 for clays + N > 10 for calcite particles). **(b)** Examples of micro stylolites and their link with porous zones. **(c)** Detailed image of stylolite connected with a porous zone containing siliceous particles and clay minerals.

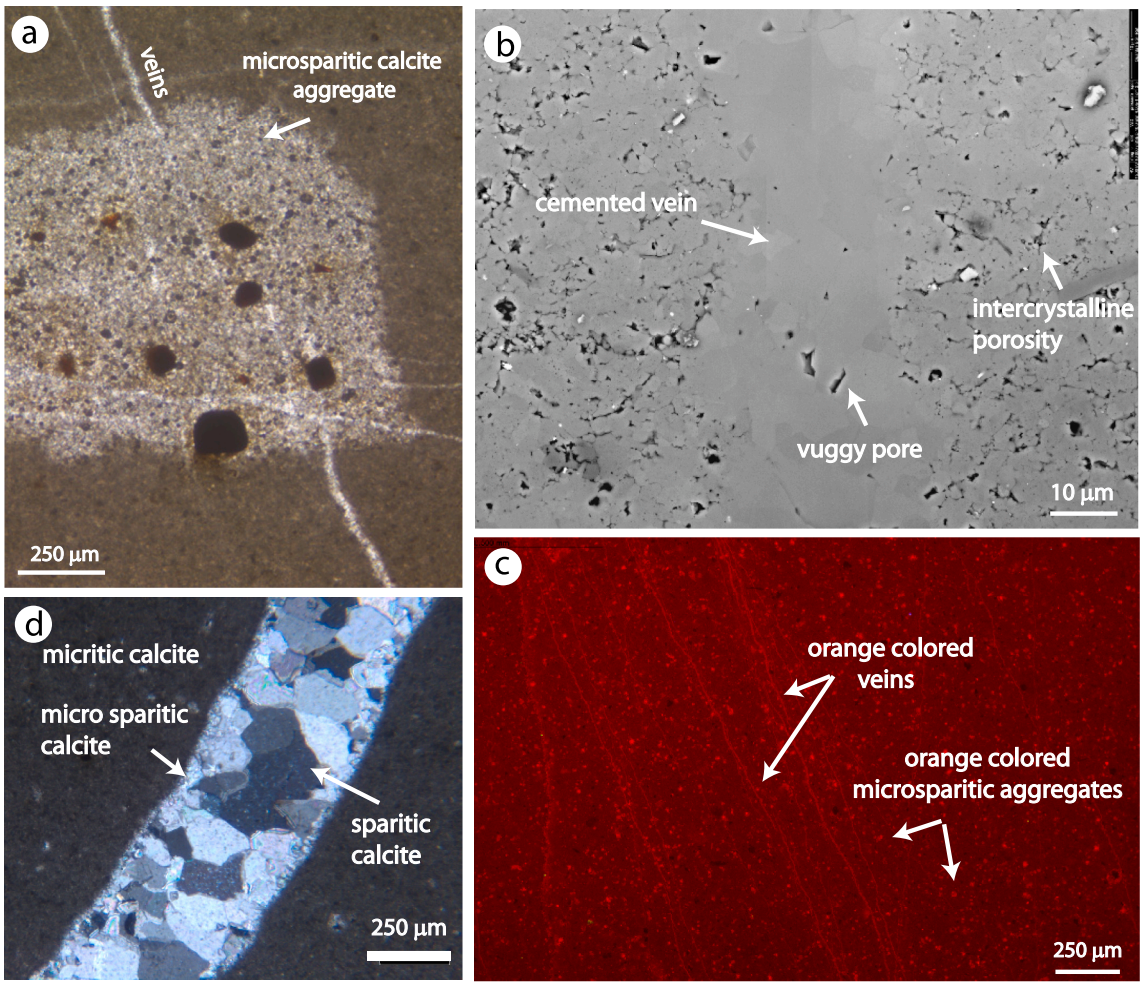

Fig. 7. Vein microstructures. **(a)** Microphotograph (*PPL* mode) showing veins crosscutting an aggregate of microsparitic calcite containing iron oxide grains. **(b)** Backscattered *SEM* image of a cemented vein. **(c)** Image (*CL* mode) of several orange veins. **(d)** Microphotograph (*CPL* mode) of a vein cement. (For interpretation of the references to color in this figure legend, the reader is referred to the Web version of this article.)

rock. This suggests no significant difference of chemical composition between vein infilling and the host rock.

In thick veins (thicker than 20 µm), a drusic fabric is observed (Beach, 1977), with microsparitic calcite crystals observed along the vein margins whereas larger sparitic calcite crystals fill the center of the vein (Fig. 7d). The microsparitic crystals are elongated normally to the vein margin and show a front of crystal facets (automorphic shapes) in the direction of the center of the vein. These crystals show an orange cathodoluminescence color similarly than narrow veins. The sparitic crystals are organized in blocky morphology or, less commonly, in elongated blocky arrangement (following the classification of Bons et al., 2012). In such case, the crystal elongation is normal to the vein wall. These crystals show the same cathodoluminescence or are slightly darker than the microsparitic crystals at the margins.

4.2.4. *Interaction between stylolites and veins*

Where the veins are connected to stylolites (Fig. 8), they are thicker next to the stylolitic surface, and their thickness progressively decreases to a few mm to cm away from the stylolite (Fig. 8a and b). The vein thickness is generally lower than 100 µm, down to 10 µm for a large majority of them (Fig. 8c). These veins strike along two main directions: N160-175°E and N0-5°E (Fig. 8d). The similar cathodoluminescence color and the crosscutting relationship between veins without displacement suggest a contemporaneous formation, with no polyphase event of veins formation.

Where the veins are specifically branched to the stylolite tip or connecting two neighboring stylolites, a more complex interaction is observed between both structures, similar to the stylolite – vein pattern at the macroscopic scale (Fig. 8e): the vein can stop at the stylolite contact (1), can be divided into several small veins (2), or can show no disturbance at the stylolite contact (3). The stylolites can stop (4) or are reoriented (5) when reaching the vein. In this example, a complex architecture of the vein infilling is observed with several stands of blocky calcite crystals which suggest polyphase opening of the vein (Fig. 8e).

4.3. *Evolution of host rock properties around stylolites and veins*

In this section, we compare the grain characteristics and porosity of the host rock away and in closed vicinity of stylolites and veins in order to evaluate the localization of deformation processes.

4.3.1. *Evolution of grain characteristics around stylolites and veins*

The *EBSD* maps reveal no change in the shape, size, deformation and orientation of the calcite grains in the areas surrounding stylolites and veins relative to the undeformed host rock (Fig. 9a). A very weak *CPO* was generally identified from pole figures in the host rock areas, with a low *M.U.D.* value ranging from 1.2 to 1.51 for the [0001] c axis (Fig. 9b–Table 1). The *J-index* is very low, ranging from 1.01 to 1.04 (Table 1). The areas surrounding stylolite and vein show preferred orientations similar to that in the host rock, and the *M.U.D.* value of these pole figures is also low, ranging from 1.19 to 1.43 (Fig. 9b). The *J-index* is also very low, ranging from 1.01 to 1.08 (Table 1). The *GOS* is low,

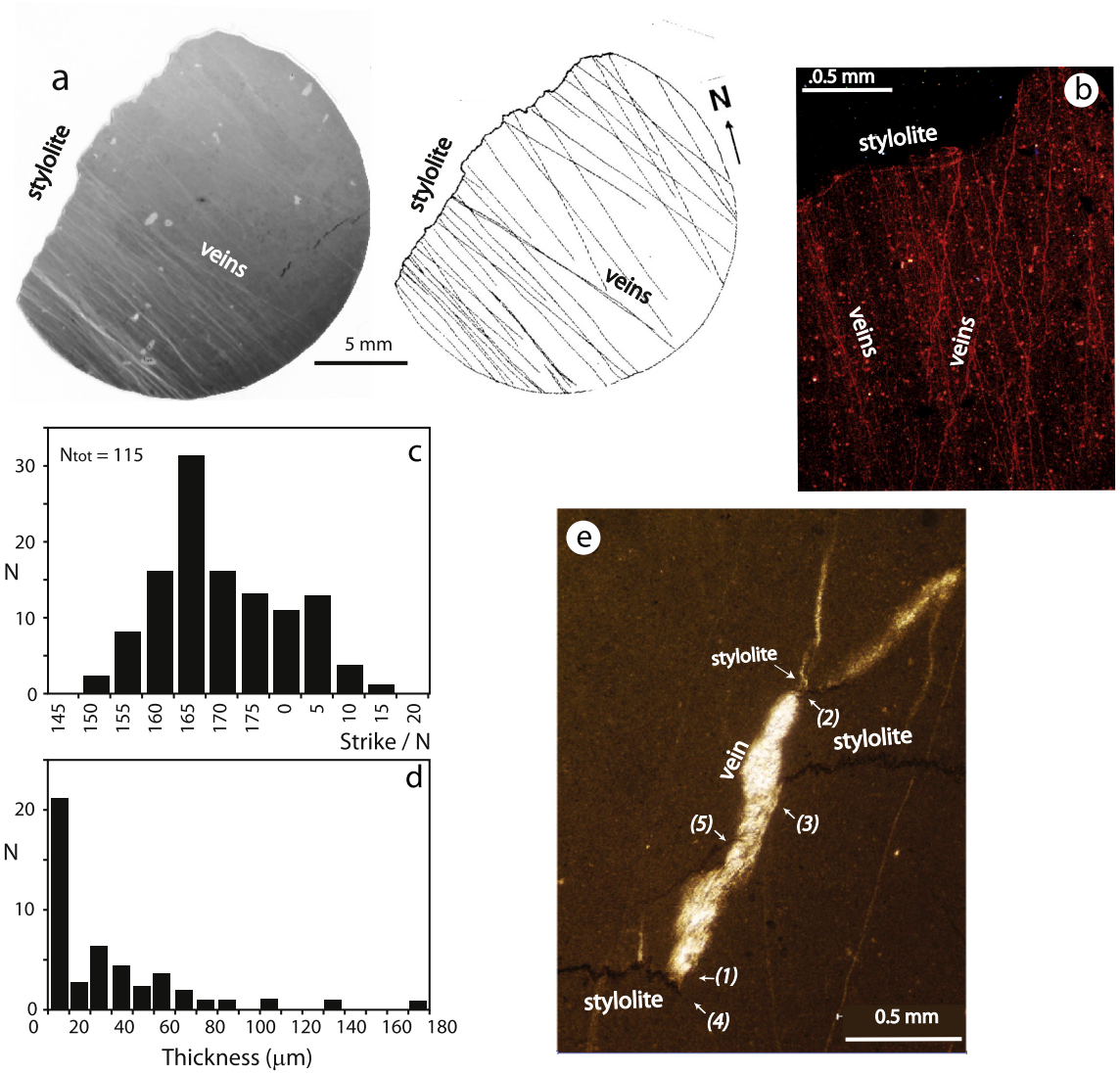

Fig. 8. Microstructural relationship between stylolites and veins. **(a)** Photography and interpretative scheme of core affected by stylolites and connected veins. **(b)** *CL* image showing the same stylolite-vein system. **(c) (d)** Graphs showing the distribution of veins orientation and thickness, respectively (from the example of Fig. 8a). **(e)** Microphotograph (*PPL* mode) of a thick vein formed between stylolite tips.

ranging from 0.41 to 0.46 for the stylolitic zones and from 0.40 to 0.45 for material surrounding veins, whereas the average *GOS* is of 0.40 for the host rock (Table 1). Hence, no significant change of preferred crystallographic orientation or internal grain deformation is detected around stylolite and vein in comparison with the undeformed host rock. Conversely, no significant change of calcite twin density, defined mainly by a rotation of approximately 78° around the <20–21> directions, is observed close to stylolites and veins compare to the host rock. We also note that no significant changes of the mineralogical composition of the host rock are observed both in the close vicinity of veins and stylolites, and out of the deformation zones.

Using the *EBSD* maps, the grain size (i.e., the grain diameter of the equivalent circle) of the host rock is on average of 2.17 ± 1.06 μm whereas the grain size of the material surrounding stylolites and veins ranges from 2.06 ± 0.98 μm to 2.24 ± 1.07 μm, and from 2.18 ± 1.06 μm to 2.22 ± 1.12 μm, respectively (Fig. 9c–Table 1). The grain shape, quantified using the grain aspect ratio (i.e., major axis a/minor axis b of the best-fit ellipse), is on average of 1.62 ± 0.46 for the host rock and ranges 1.59 ± 0.43 to 1.66 ± 0.50, and from 1.59 ± 0.43 to 1.73 ± 0.56 for material surrounding stylolites and veins, respectively (Fig. 9d–Table 1). These results show that no significant grain size and shape modification is detected in the host rock close to the deformation structures; all the deformation occurs within the stylolite - vein system.

4.3.2. *Porosity evolution around stylolites and veins*

A connected porosity of 0.17% and 1.34% was measured by the *MIP* method in the host rock samples (Fig. 10a, bed 6 and 14). Pore access radii lower than 0.015 μm were measured with median pore access radii of 0.0043 μm and 0.006 μm for these two samples (Table 2). A low value of permeability is obtained, ranging from 10^{-4} and 10^{-6} mD (10^{-20} and 10^{-22} m^2). The three other host rock samples were not intruded by mercury; their pore access radii are then lower than 0.0037 μm and connected porosity close to 0.

Samples containing stylolites have porosity values ranging from 0.9% to 1.7%. These values are similar to, or slightly higher than those of the host rocks. The distribution of pore access radii shows porosity is mainly connected by pore access radii smaller than 0.013 μm, which is comparable to the host rock (Table 2). However, two additional ranges of larger pore access radii contribute to the porosity, from 4 μm to 12 μm and from 0.039 μm to 0.12 μm (Fig. 10b). A slightly higher permeability is obtained, ranging from 1.09 10^{-4} to 4.23 10^{-4} mD (≈1.08 10^{-19} to 4.17 0^{-19} m^2), compared to the host rock.

Samples containing veins have porosity values ranging from 1.4% to 1.76%. These values are similar to, or slightly higher, than those of the

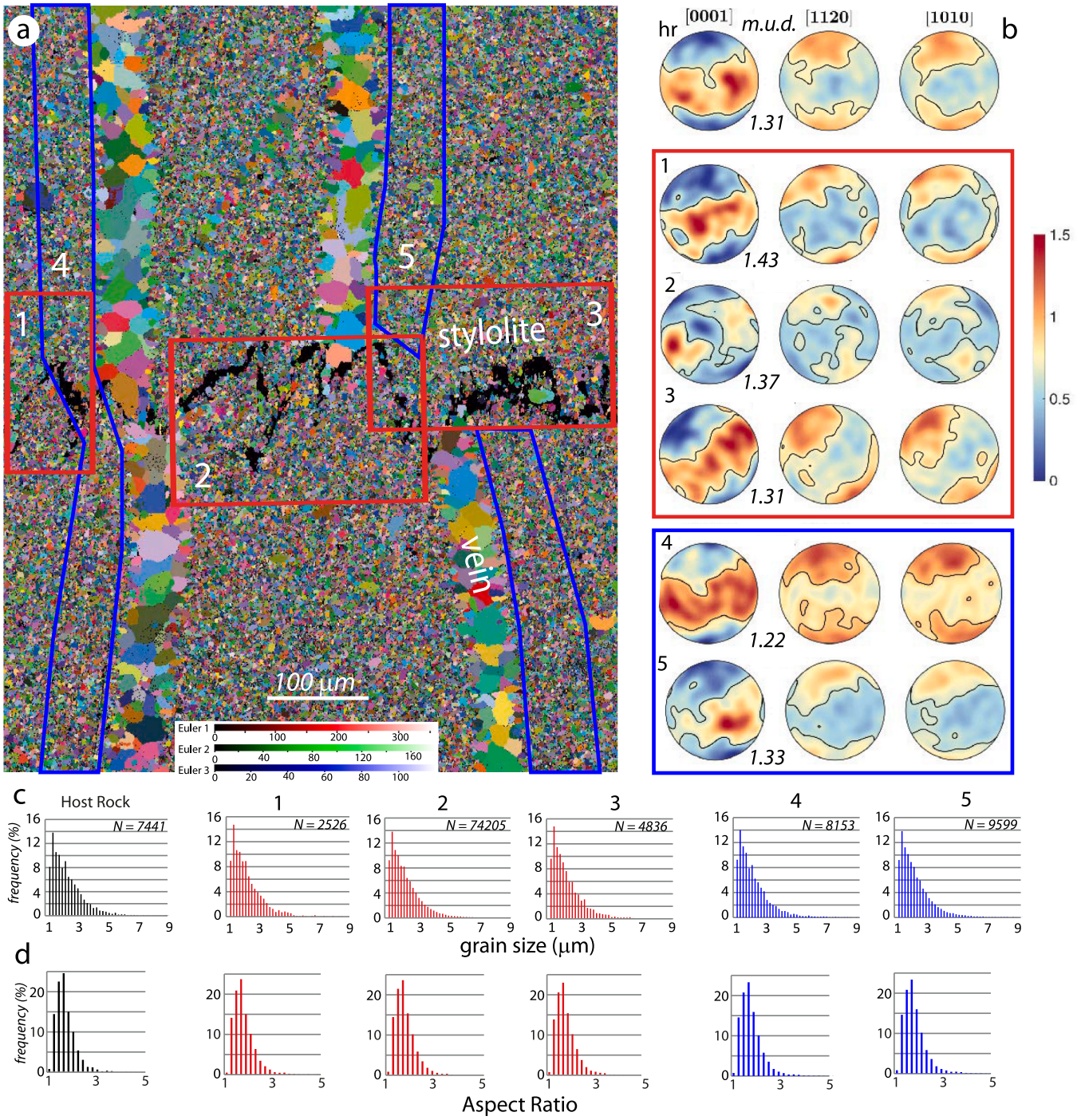

Fig. 9. *EBSD* data on an example of vein-stylolite zone. **(a)** All Euler map showing the detected grains (each colored area represents an individual grain with its mean orientation, the color is coded with respect to its Euler angles). **(b)** Pole figures showing the crystallographic preferred orientation (*CPO*) of calcite grains. The *m. u.d.* Value is also reported for each [0001] pole figure. **(c)** Graphs showing the distribution of grain size for the different domains numbered in (a). **(d)** Graphs showing the distribution of the grain aspect ratio for the different study domains numbered in (a). (For interpretation of the references to color in this figure legend, the reader is referred to the Web version of this article.)

host rock. The distribution of pore access radii shows porosity mainly connected by pore access radii smaller than 0.013 µm, which is comparable to that of the host rock (Table 2). However, two additional ranges of larger pore access radii contribute to the porosity, i.e. from 3 µm to 7.7 µm and from 0.049 µm to 0.077 µm (Fig. 10c). The calculated permeability ranges from 2.12 10^{-2} to 7.00 10^{-5} mD (≈2.09 10^{-17} to 6.91 10^{-20} m^2), comparable to that of the host rock or significantly higher. The measured deformed samples integrate a large part of host rock.

To remove the impact of the host rock on the evaluation of the porosity characteristics of the stylolites and veins, and better constrain the location of the porosity change, porosity values were estimated from *SEM-BSE* image analysis along transects perpendicular to stylolites and veins. These transects show a porosity ranging from 0.19% to 2.87% in the host rock (Fig. 11a and b). Porosity ranges from 4% to 22% in images containing a part of a stylolite but such high porosity values have to be

Table 1
Summary of the different grain parameters obtained from *EBSD* data. *N* is the number of analyzed grains on each acquisition. The *GOS* represents the internal deformation of grain. The max *m.u.d.* (multiple of the uniform distribution) and the *J-index* represent the intensity of the crystallographic preferred orientations.

type	N	Grain Size (μm)		Aspect Ratio		GOS		m.u.d.	J
		Mean	Median	Mean	Median	Mean	Median	Max	
HR	*32 839*	2,26 ± 1,12	1,95	1,59 ± 0,42	1,51	0,41 ± 0,47	0,31	1,2	1,01
HR	*4624*	2,24 ± 1,21	1,94	1,62 ± 0,52	1,52	0,38 ± 0,43	0,3	1,51	1,04
HR	*7441*	2,24 ± 1,05	1,97	1,57 ± 0,41	1,49	0,38 ± 0,40	0,3	1,31	1,03
HR	*7240*	2,07 ± 0,98	1,78	1,63 ± 0,45	1,54	0,45 ± 0,48	0,35	1,41	1,03
HR	*20 433*	2,14 ± 0,99	1,87	1,67 ± 0,49	1,56	0,39 ± 0,42	0,3	1,29	1,02
HR	*4650*	2,07 ± 0,98	1,78	1,61 ± 0,44	1,52	0,41 ± 0,48	0,31	1,36	1,04
mean		**2,17 ± 1,06**	**1,88**	**1,62 ± 0,46**	**1,52**	**0,40 ± 0,45**	**0,31**	**1,35**	**1,03**
S.	*4836*	2,19 ± 1,06	1,88	1,62 ± 0,47	1,52	0,43 ± 0,44	0,33	1,31	1,08
S.	*5707*	2,24 ± 1,07	1,95	1,59 ± 0,43	1,51	0,41 ± 0,45	0,32	1,37	1,06
S.	*2526*	2,20 ± 1,07	1,93	1,61 ± 0,48	1,51	0,41 ± 0,41	0,32	1,43	1,07
S.	*13 388*	2,09 ± 0,98	1,8	1,66 ± 0,50	1,55	0,46 ± 0,47	0,35	1,19	1,01
S.	*10 413*	2,06 ± 0,98	1,8	1,61 ± 0,44	1,52	0,45 ± 0,48	0,34	1,25	1,02
V.	*8153*	2,22 ± 1,12	1,93	1,60 ± 0,44	1,51	0,40 ± 0,45	0,31	1,22	1,02
V.	*9599*	2,18 ± 1,03	1,9	1,59 ± 0,43	1,51	0,43 ± 0,46	0,31	1,33	1,02
V.	*6046*	2,18 ± 1,06	1,89	1,69 ± 0,52	1,57	0,44 ± 0,48	0,32	1,33	1,03
V.	*6869*	2,20 ± 1,10	1,89	1,73 ± 0,56	1,6	0,42 ± 0,49	0,31	1,34	1,03

considered with caution because they integrate clay material accumulated in the stylolite zones. The porosity immediately drops down to the host rock values away from the stylolite (Fig. 11b). These transects reveal no progressive change of porosity at the stylolite contact whereas the high values of stylolite porosity are only related to processes occurring within the stylolite. As previously mentioned, the porosity is lower inside the veins than in the surrounding host rock. For example, in Fig. 8c the average vein porosity is 0.39%, whereas the porosity of surrounding rock ranges from 2.19% to 2.87%. The porosity of veins is formed by vuggy pores between calcite crystals. These pores are generally observed in the central part of veins.

5. Discussion

5.1. Role of clay for the initiation of pressure-solution

Since the studied stylolites are related to micropore spaces, the intercrystalline micropores disseminated in the matrix play a major role on the stylolite occurrence in such low-porosity rock ($\varphi < 1.5\%$, Fig. 10a). The origin of this microporosity is then of first importance for the stylolite initiation. The origin of the microporosity can be linked to the disseminated clays, by a porosity preservation during early diagenesis or specific clays diagenesis during burial. The mixed-layer illite-smectite that has a relatively high average charge (0.6–0.7) indicates a low amount of smectite layers in the interstratified minerals, and an efficient illitization during diagenesis of limestones initially containing smectite (Fig. 6a). A proportion of <2% of clay disseminated in the host rock then contributes to trigger the initiation of pressure-solution in low-porosity limestone. This is consistent with the numerous studies that underline the importance of clays on pressure-solution initiation and stylolite density (Marshak and Engelder, 1985; Bathurst, 1987; Andrews and Railsback, 1997; Renard et al., 2001; Vandeginste and John, 2013; Paganoni et al., 2016), and confirms that a few percent of clays are enough to promote pressure-solution (Renard et al., 2001; Rustichelli et al., 2012). Fluid release and porosity creation during clay diagenesis, such as the smectite-illite conversion during burial (Dunoyer De Segonzac, 1970; Hower et al., 1976; Meng et al., 2021), instigate favorable conditions to trigger stylolite-initiation during late basin inversion (Fig. 12a). This process could be added to other processes related to clays that trigger pressure-solution: clays form a water film at their surface that provides numerous diffusion paths in the host rock (Heald, 1959; Renard et al., 1997); clays form an interconnected network between sites of dissolution to the free fluid phase in the rock (for a proportion a clay-quartz matrix >10%, Marshak and Engelder, 1985); clays increase the mineral solubility (Walderhaug et al., 2004; Greene et al., 2009); and clays enhance dissolution on the stylolite flanks (Meyer et al., 2006; Aharonov and Katsman, 2009). Since smectite is described as abundant in pelagic micritic or argillaceous limestones (Chamley, 2013), such diagenetic evolution and its related triggering impact on the formation of tectonic stylolite is potentially frequent and deserves to be checked on additional examples. The abundance of pervasively distributed networks of tectonic Layer Parallel Shortening (*LPS*) stylolites described in such low-porosity clayey mudstones could be consistent with the present process (Alvarez et al., 1976; Tavani et al., 2010).

5.2. A model of tectonic stylolite-vein system formation in low-porosity limestone

The mutual connection, reorientation or disturbance between veins and stylolites (Figs. 3 and 8) suggest a synchronous formation of both structures in a closed system of deformation and related material transfers. The orthogonal veins and stylolites are both vertical (i.e., perpendicular to the bedding), and formed as *LPS* structures under the strike-slip regime related to the sub-horizontal North-South Pyrenean compression (Petit and Mattauer, 1995; Maerten et al., 2016). Because the stylolites and related veins never propagate in adjacent limestone beds, the deformation is accommodated bed by bed and the origin of fluid cannot be external.

The organization of the stylolite–vein system described in the present study differs from the classical model of tectonic stylolite-vein system formation, which generally starts with the development of en-echelon veins followed by the formation of subsequent stylolites (Peacock and Sanderson, 1995; Willemse et al., 1997; Crider and Peacock, 2004). In such classical context, the fluids and porosity are supplied by the vein opening combined with the increase of pressure along the vein border that favor pressure-solution, and explain why the stylolite amplitude increases next to the vein or the fault plane (Fletcher and Pollard, 1981; Smith, 2000; Benedicto and Schultz, 2010; Zhou and Aydin, 2012).

In the present example, the stylolite-vein system starts with the initiation of pressure-solution at micropores and forms microsegments linking neighboring pore spaces (Fig.. 6c and 12b). These early stages are followed by the connection of small stylolite segments (Fig. 6b), and their incorporation to the main stylolitic interface as suggested by the presence of abandoned peaks (Fig. 5c). The segmentation of the stylolites during their early stages of development was already described in sandstone (Nenna and Aydin, 2011), but remains poorly documented in limestones. This process certainly impacts the stylolite morphology and roughness, and could be at the origin of the variable wavelength of peaks observed along such structure (Fig. 5b). In a second stage segment

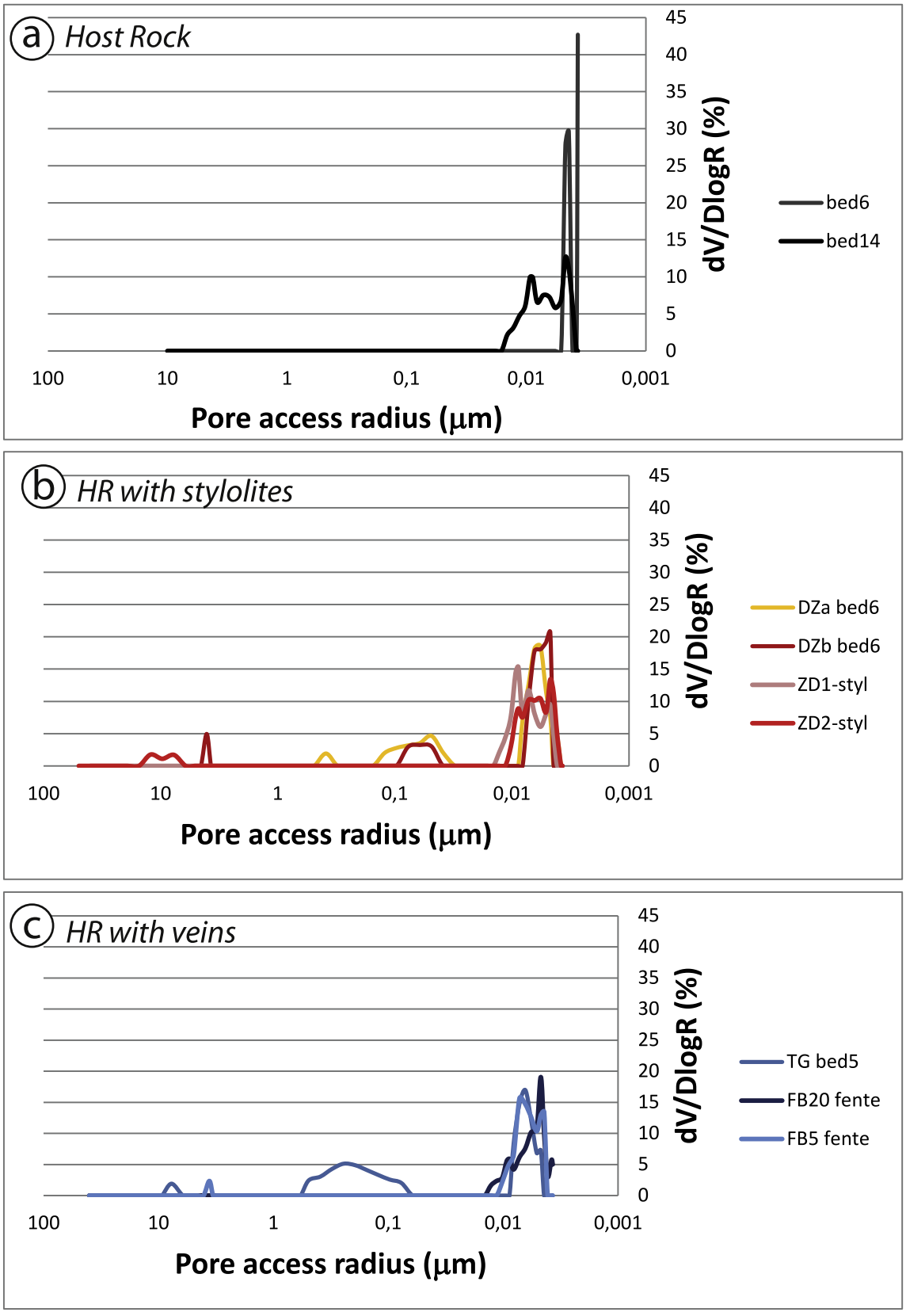

Fig. 10. Graph showing the pore access radii distribution of the underformed host rock **(a)**, sample containing stylolites **(b)**, and sample containing veins **(c)**.

Table 2
Summary of porosity values, median pore radius, range of pore access radius, and permeability from Mercury Injection Porosimetry for undeformed host rock samples, samples with stylolites and samples with veins.

type	sample	connected Porosity (%)	median pore radius (μm)	Range of pore access radius (μm)			permeability (mD)
Host Rock	*B5*	0.07	x	no intrusion (>0.0037)			x
	B6	0.17	0.0044			0.0047–0.0037	4.11E-06
	B14	1.33	x			0.0144–0.0041	x
	B15.1	0.36	x	no intrusion (>0.0037)			x
	B15.4	0.35	0.0083	no intrusion (>0.0037)			3.01E-05
w. Stylolites	*ZD1*	1.7	0.0085			0.013–0.0044	1.54E-04
	ZD2	1.46	0.00772	12.2–7.7		0.010–0.0041	1.09E-04
	ZB_1B	0.91	0.0103	4.05	0.0769–0.049	0.007–0.0047	1.21E-04
	ZD_1A	1.34	0.0159		0.122–0.039	0.008–0.0041	4.23E-04
w. Veins	*FB5*	1.76	0.0072	3.4		0.010–0.0044	1.14E-04
	FB20	1.41	0.0063			0.013–0.0037	7.00E-05
	ZD_B5	1.55	0.1046	7.7	0.49–0.077	0.008–0.0047	2.12E-02

connection occurs at the macroscale, when stylolites are longer than ~1 m.

The lack of host rock deformation in areas surrounding stylolites reveals that pressure solution is strictly restricted to the stylolite interface, and that no dissolved material is evacuated to the surrounding porosity. This result differs from the example described by Ebner et al. (2010) where a grain size reduction of 15–25% and a significant *CPO* were detected over a few tens of μm near the stylolite, revealing a diffuse zone of pressure-solution. This model also differs from the stylolite initiation and growth proposed by Carrio-Schaffhauser et al. (1990). In that model, an increase of grain dissolution and high-porosity zones is described as damage zones developed around the main stylolitic interface. A preferential cementation of these high-porosity damage zones can finally occur and clog the pore space (Raynaud and Carrio-Schaffhauser, 1992; Hou et al., 2023). These "damage" models assume a different dissolution, transport and precipitation pattern following a hydraulic-chemical-mechanical feedback loop surrounding the stylolite core zone (Merino et al., 1983). The difference in host rock porosity, or the occurrence of different secondary diagenetic processes (for example the formation of pyrite and the implication of external fluids in Hou et al., 2023), lead to different ways of stylolite initiation and growth. In any case, the characteristics of the host material, i.e., the porosity properties, the localization of fluids, and the presence of heterogeneity in the grain framework, will govern both the pressure-solution initiation and the model of stylolite development.

The calcite cement infilling the veins shows a syntaxial growth: vein-filling minerals grow out from the wall rock of the vein, generally into an open fluid-filled space (Bons et al., 2012). This texture argues for fast vein opening and a large impact of the fluids on this mechanism (Beach, 1977; de Joussineau et al., 2005). Since the pore access radii are too small in the surrounding rock to allow fluids to escape from the stylolite zone, the compaction by pressure-solution can induce fluid overpressure along the stylolite interface. This local fluid overpressure is responsible for the decrease of the mean effective stress that can reach the hydraulic fracturing field leading to dilatant vein initiation (Fig. 12c). Hence, veins appear to be mainly triggered by local fluid overpressure along the stylolite, additionally to the tectonic stress field that governs their general trending (Fig. 3b). In this sense, the veins can be considered as hybrid hydraulic-tectonic fractures in a system with local high fluid pressure, owing to their orientation with respect to far-field principal stress (Bons et al., 2022). The connection of veins to the stylolite interface, and their wing crack morphology are consistent with this process (Nelson, 1981). The fluid overpressure is then released during vein opening and cementation (Laronne Ben-Itzhak et al., 2014), contemporaneously with the desaturation of fluids with respect to dissolved calcium, leading to a new increase of the mean effective stress, and to the return of the pressure-solution mechanical conditions along the stylolite. The vein initiation could also be favored by the heterogeneity of the stylolite interface (morphology, composition), causing local stress perturbations (Eren, 2005; Zhou and Aydin, 2012; Aharonov and Karcz, 2019), or by a local non-uniform stress field caused by the dissolution occurring in the stylolite within a solid rock (Katsman, 2010). After vein cementation, the fluid pressure can increase again along the stylolite interface (Fig. 12c). The lack of evidence for reopening events in narrow veins suggests that their cementation leads to a local strengthening of the rock. The lack of microporosity in the veins and the cohesion between cement and vein walls argue for this strengthening process. Hence, the opening of a new vein is necessary to accommodate the fluid overpressure along the stylolite interface during the compression stage.

The lack of porosity change (Figs. 10 and 11) and of variations in grain size, shape or misorientation (Fig. 9) around stylolites, coupled with the homogeneity of cathodoluminescence in the different veins (Fig. 7), reveal that the system of material transfer from dissolution zone to cementation one is closed, and no external fluids are integrated in the system. This is mainly due to the low permeability of the host rock that impedes the evacuation of the dissolved material in the surrounding matrix areas. Hence we can consider that the volume of cementation in veins corresponds to the volume of dissolved material along the connected stylolites, and could be used to estimate the amount of shortening occurring by pressure-solution in such lithological context (Delair and Leroux, 1978; Carrio-Schaffhauser and Chenevas-Paule, 1989).

The stylolite-vein system grows progressively by stylolite lateral propagation and related vein formation on individual stylolites. The system progressively turns into a more complex pattern where connection processes occur between two surrounding stylolites or where a stylolite propagation reaches a preexisting vein formed from another stylolite (Fig.. 3d and 8e). In such zones, stylolite reorientation or termination can occur whereas the veins can show evidences of polyphased opening and cementation. The system appears to reach a stage of ultimately saturation as suggested by the regular spacing observed between stylolites, the whole connection between surrounding stylolites and veins, and the length to amplitude relationship measured on individual stylolite.

6. Conclusions

The detailed study of the stylolite-vein system formed in the Les Matelles limestone allowed us to understand how tectonic stylolite can initiate and grow in low-porosity rock, and why vein opening is necessary in this deformation process. Our study reveals the key role of microporosity and fluid release, potentially related to the clay mineral transformation (smectite-illite conversion), on the initiation of pressure-solution processes in the context of low-permeability host rock and *LPS* setting. After micro-stylolite initiation in slightly more porous volumes and stylolite segment connection, the stylolites progressively grow with

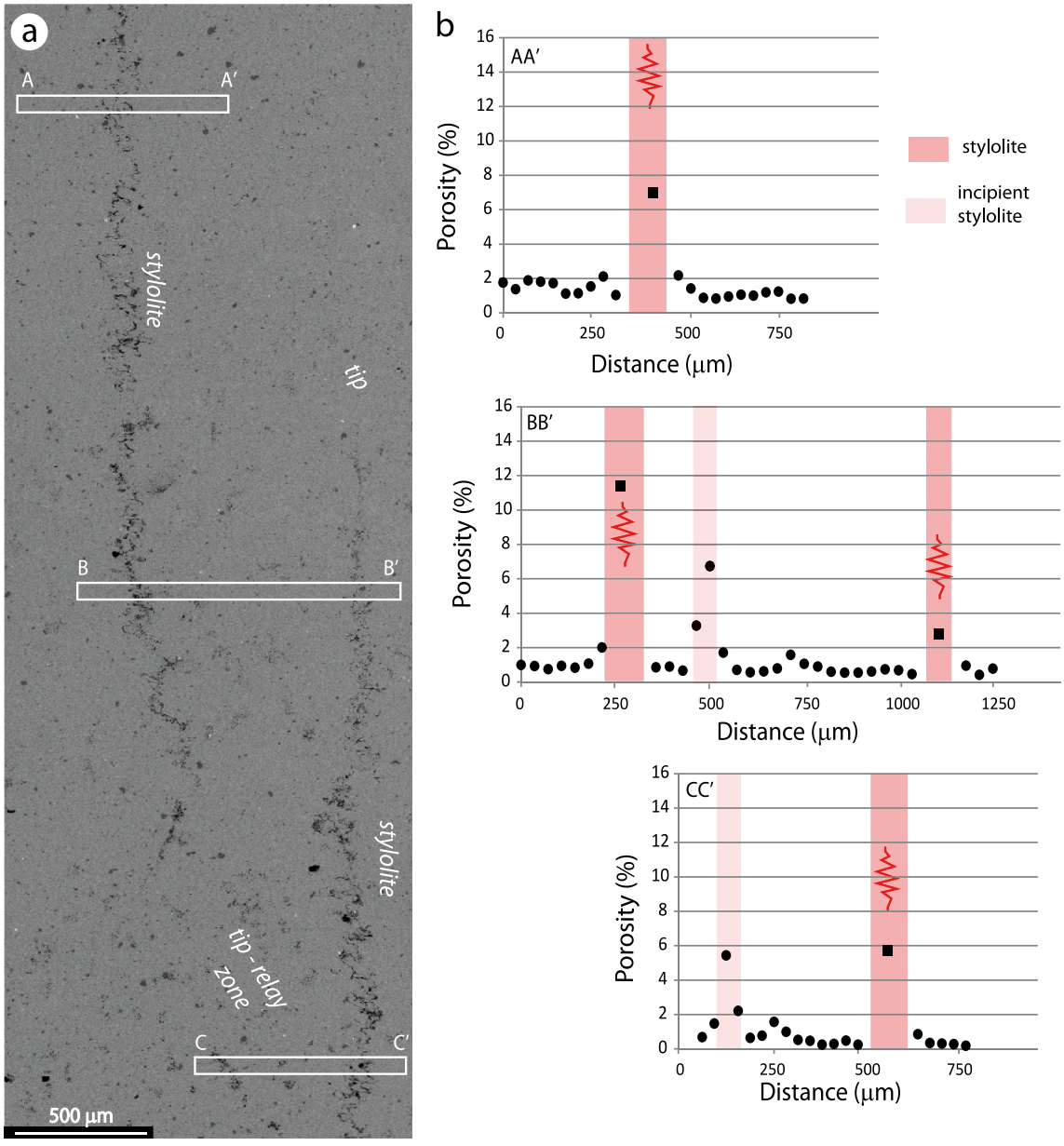

Fig. 11. Evolution of host rock porosity across stylolites. **(a)** *SEM-BSE* image showing an example of a relay zone between two stylolites. The white rectangles indicate the location of the different transects of porosity estimates. **(b)** Graphs showing the evolution of porosity along the different transects in (a). The red parts represent the stylolite zones. A threshold value of grey shade of 70 is used to separate the pore space from the grains. (For interpretation of the references to color in this figure legend, the reader is referred to the Web version of this article.)

the assistance of perpendicular veins opening, triggered by fluid overpressure along the stylolitic interface. This fracturing process is due to the very low porosity of the host rock, impeding the evacuation of dissolved material to the surrounding matrix. The dissolved material is transported to the opened vein, which is then infilled by calcite cement, clogging the newly formed pore space. The cementation of the vein leads to a new increase of fluid pressure along the stylolite, triggering a new vein formation. This deformation process forms a closed system of material transport from the dissolved zones (the stylolitic interface) to the precipitation zones (the opened veins), without diffuse deformation or cementation in the host rock surrounding deformation structures. It is mainly controlled by the low porosity of the host rock and specific diagenetic processes related to clay transformation. This model differs from stylolite development and stylolite-vein interaction described in other geological contexts and completes the range of models proposed to explain them. Clay diagenesis as a process instigating favorable conditions for pressure-solution initiation in low-porosity micritic mudstone deserves further investigation.

CRediT authorship contribution statement

Grégory Ballas: Conceptualization, Data curation, Formal analysis, Funding acquisition, Investigation, Methodology, Project administration, Resources, Writing – original draft, Writing – review & editing. **Suzanne Raynaud:** Data curation, Formal analysis, Investigation, Methodology, Validation, Writing – original draft. **Michel Lopez:** Investigation, Supervision, Validation. **Emilien Oliot:** Formal analysis, Methodology, Software, Validation. **Jean-Pierre Sizun:** Data curation, Methodology, Validation. **Jacinthe Caillaud:** Data curation, Methodology, Validation. **Fabrice Barou:** Data curation, Methodology, Software. **Benoit Ildefonse:** Formal analysis, Methodology, Software, Supervision, Writing – review & editing.

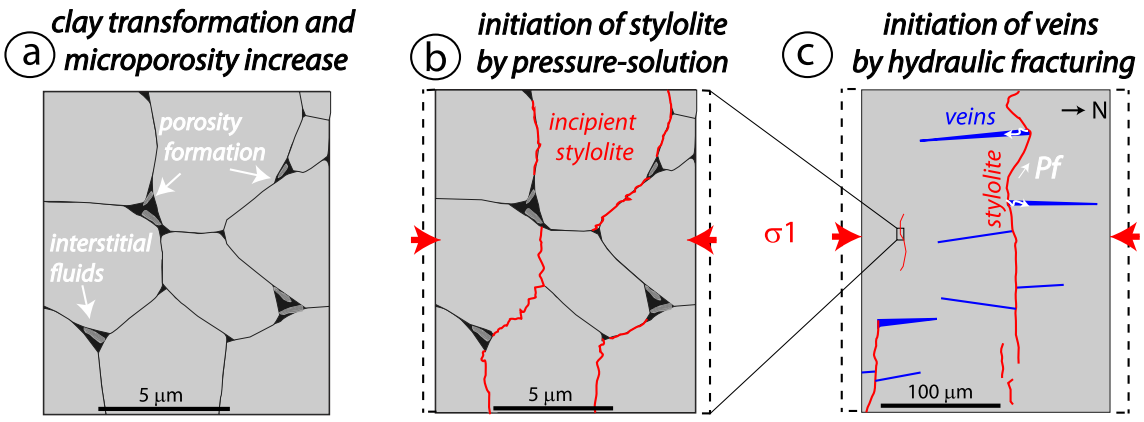

Fig. 12. Conceptual model of formation of the stylolite - vein system from the Les Matelles micritic limestone. The model is composed of 3 main stages: **(a)** Smectite-illite transformation creating microporosity and releasing interstitial fluids during late diagenesis. **(b)** Pressure-solution initiation at micropores and connection of surrounding stylolite segments during Pyrenean tectonic compression (LPS). **(c)** Pore pressure increase and vein initiation by pore fluid overpressure (hydraulic fracturing), followed by reactivation of pressure-solution in stylolite after vein clogging.

Declaration of competing interest

The authors declare that they have no known competing financial interests or personal relationships that could have appeared to influence the work reported in this paper.

Data availability

Data will be made available on request.

Acknowledgements

We acknowledge Christophe Nevado and Doriane Delmas for the thin-section preparation, and Frédéric Fernandez for his help on the *SEM* acquisitions. We thank Marion Delattre and Viviane Bout Roumazailles for the *XRD* acquisitions and Olivia Maugin for the electron probe micro-analyses. Pierre Labaume is acknowledged for his help with cath-odoluminescence microscopy. We thank Fabrizio Agosta (editor), Nic-olas Beaudoin and an anonymous reviewer for the valuable comments that significantly helped improving the manuscript.

References

Aharonov, E., Karcz, Z., 2019. How stylolite tips crack rocks. J. Struct. Geol. 118, 299–307. https://doi.org/10.1016/j.jsg.2018.11.002.

Aharonov, E., Katsman, R., 2009. Interaction between pressure solution and clays in stylolite development: insights from modeling. Am. J. Sci. 309, 607. https://doi.org/10.2475/07.2009.04.

Alvarez, W., Engelder, T., Geiser, P.A., 1978. Classification of solution cleavage in pelagic limestones. Geology 6, 263–266. https://doi.org/10.1130/0091-7613(1978)6<263:COSCIP>2.0.CO;2.

Alvarez, W., Engelder, T., Lowrie, W., 1976. Formation of spaced cleavage and folds in brittle limestone by dissolution. Geology 4, 698–701. https://doi.org/10.1130/0091-7613(1976)4<698:FOSCAF>2.0.CO;2.

Andrews, L.M., Railsback, L.B., 1997. Controls on stylolite development: morphologic, lithologic, and temporal evidence from bedding-parallel and transverse stylolites from the U.S. Appalachians. J. Geol. 105, 59–73. https://doi.org/10.1086/606147.

Andrieux, J., Mattauer, M., Tomasi, P., Martinez, C., Reille, J.-L., Matte, P., 1972. Carte géologique de la France au 1/50 000. In: Feuille de Montpellier, vol. 990.

Arthaud, F., Mattauer, M., 1969. Exemples de stylolites d'origine tectonique dans le Languedoc, leurs relations avec la tectonique cassante. Bull. de La Société Géologique de France S7-XI 738–744. https://doi.org/10.2113/gssgfbull.S7-XI.5.738.

Arthaud, F., Séguret, M., 1981. Les structures pyrénéennes du Languedoc et du Golfe du Lion (Sud de la France). Bull. Soc. Geol. Fr. S7-XXIII, 51–63. https://doi.org/10.2113/gssgfbull.S7-XXIII.1.51.

Barbarand, J., Préhaud, P., Baudin, F., Missenard, Y., Matray, J.M., François, T., Blaise, T., Pinna-Jamme, R., Gautheron, C., 2020. Where are the limits of Mesozoic intracontinental sedimentary basins of southern France? Mar. Petrol. Geol. 121, 104589.

Bathurst, R.G.C., 1995. Burial diagenesis of limestones under simple overburden; stylolites, cementation and feedback. Bull. Soc. Geol. Fr. 166, 181–192.

Bathurst, R.G.C., 1987. Diagenetically enhanced bedding in argillaceous platform limestones: stratified cementation and selective compaction. Sedimentology 34, 749–778. https://doi.org/10.1111/j.1365-3091.1987.tb00801.x.

Baud, P., Rolland, A., Heap, M., Xu, T., Nicolé, M., Ferrand, T., Reuschlé, T., Toussaint, R., Conil, N., 2016. Impact of stylolites on the mechanical strength of limestone. Tectonophysics 690, 4–20. https://doi.org/10.1016/j.tecto.2016.03.004.

Beach, A., 1977. Vein arrays, hydraulic fractures and pressure-solution structures in a deformed flysch sequence S.W. England. Tectonophysics 40, 201–225. https://doi.org/10.1016/0040-1951(77)90066-X.

Beaudoin, N., Koehn, D., Lacombe, O., Lecouty, A., Billi, A., Aharonov, E., Parlangeau, C., 2016. Fingerprinting stress: stylolite and calcite twinning paleopiezometry revealing the complexity of progressive stress patterns during folding—the case of the Monte Nero anticline in the Apennines, Italy. Tectonics 35, 1687–1712. https://doi.org/10.1002/2016TC004128.

Beaudoin, N., Lacombe, O., 2018. Recent and future trends in paleopiezometry in the diagenetic domain: insights into the tectonic paleostress and burial depth history of fold-and-thrust belts and sedimentary basins. J. Struct. Geol. 114, 357–365. https://doi.org/10.1016/j.jsg.2018.04.001.

Beaudoin, N.E., Labeur, A., Lacombe, O., Koehn, D., Billi, A., Hoareau, G., Boyce, A., John, C.M., Marchegiano, M., Roberts, N.M., Millar, I.L., Claverie, F., Pecheyran, C., Callot, J.-P., 2020. Regional-scale paleofluid system across the Tuscan Nappe–Umbria–Marche Apennine Ridge (northern Apennines) as revealed by mesostructural and isotopic analyses of stylolite–vein networks. Solid Earth 11, 1617–1641. https://doi.org/10.5194/se-11-1617-2020.

Benedicto, A., Schultz, R.A., 2010. Stylolites in limestone: magnitude of contractional strain accommodated and scaling relationships. Faulting and fracturing of carbonate rocks: new insights into deformation mechanisms. Petrophys. Fluid Flow Prop. 32, 1250–1256. https://doi.org/10.1016/j.jsg.2009.04.020.

Bons, P.D., Cao, D., de Riese, T., González-Esvertit, E., Koehn, D., Naaman, I., Sachau, T., Tian, H., Gomez-Rivas, E., 2022. A review of natural hydrofractures in rocks. Geol. Mag. 159, 1952–1977. https://doi.org/10.1017/S0016756822001042.

Bons, P.D., Elburg, M.A., Gomez-Rivas, E., 2012. A review of the formation of tectonic veins and their microstructures. J. Struct. Geol. 43, 33–62. https://doi.org/10.1016/j.jsg.2012.07.005.

Bout-Roumazeilles, V., Cortijo, E., Labeyrie, L., Debrabant, P., 1999. Clay mineral evidence of nepheloid layer contributions to the Heinrich layers in the northwest Atlantic. Palaeogeogr. Palaeoclimatol. Palaeoecol. 146, 211–228. https://doi.org/10.1016/S0031-0182(98)00137-0.

Braithwaite, C.J.R., 1989. Stylolites as open fluid conduits. Mar. Petrol. Geol. 6, 93–96. https://doi.org/10.1016/0264-8172(89)90078-0.

Bruna, P.-O., Lavenu, A.P.C., Matonti, C., Bertotti, G., 2018. Are stylolites fluid-flow efficient features? J. Struct. Geol. https://doi.org/10.1016/j.jsg.2018.05.018.

Bunge, H.-J., 2013. Texture Analysis in Materials Science: Mathematical Methods. Elsevier.

Bussolotto, M., Benedicto, A., Moen-Maurel, L., Invernizzi, C., 2015. Fault deformation mechanisms and fault rocks in micritic limestones: examples from Corinth rift normal faults. J. Struct. Geol. 77, 191–212. https://doi.org/10.1016/j.jsg.2015.05.004.

Carozzi, A.V., Bergen, D.V., 1987. Stylolitic porosity in carbonates: a critical factor formation for deep hydrocarbon production. J. Petrol. Geol. 10, 267–282. https://doi.org/10.1111/j.1747-5457.1987.tb00946.x.

Carrio-Schaffhauser, E., Chenevas-Paule, F., 1989. Quantification geometrique de la dissolution-cristallisation lies a une deformation cassante. Bull. Soc. Geol. Fr. V, 597–604. https://doi.org/10.2113/gssgfbull.V.3.597.

Carrio-Schaffhauser, E., Raynaud, S., Latière, H.J., Mazerolle, F., 1990. Propagation and localization of stylolites in limestones. Geol. Soc., London, Spec. Publ. 54, 193. https://doi.org/10.1144/GSL.SP.1990.054.01.19.

Chamley, H., 2013. Clay Sedimentology. Springer Science & Business Media.

Choukroune, P., 1969. Un exemple d'analyse microtectonique d'une série calcaire affectée de plis isopaques ("concentriques"). Tectonophysics 7, 57–70. https://doi.org/10.1016/0040-1951(69)90064-X.

Crider, J.G., Peacock, D.C.P., 2004. Initiation of brittle faults in the upper crust: a review of field observations. J. Struct. Geol. 26, 691–707. https://doi.org/10.1016/j.jsg.2003.07.007.

de Joussineau, G., Bazalgette, L., Petit, J.-P., Lopez, M., 2005. Morphology, intersections, and syn/late-diagenetic origin of vein networks in pelites of the Lodève Permian Basin, Southern France. J. Struct. Geol. 27, 67–87. https://doi.org/10.1016/j.jsg.2004.06.016.

Delair, J., Leroux, C., 1978. Methodes des quantification de la disparition de matiere au niveau de stylolites tectoniques et mechanismes de la deformation cassante des calcaires. Bull. Soc. Geol. Fr. S7-XX, 137–144. https://doi.org/10.2113/gssgfbull.S7-XX.2.137.

Dunnington, H.V., 1967. Aspects of diagenesis and shape change in stylolitic limestone reservoirs. In: Presented at the 7th World Petroleum Congress. WPC-12129.

Dunoyer De Segonzac, G., 1970. The transformation of clay minerals during diagenesis and low-grade metamorphism: a review. Sedimentology 15, 281–346. https://doi.org/10.1111/j.1365-3091.1970.tb02190.x.

Ebner, M., Piazolo, S., Renard, F., Koehn, D., 2010. Stylolite interfaces and surrounding matrix material: nature and role of heterogeneities in roughness and microstructural development. J. Struct. Geol. 32, 1070–1084. https://doi.org/10.1016/j.jsg.2010.06.014.

Eren, M., 2005. Origin of stylolite related fractures in Atoka Bank Carbonates, Eddy County, New Mexico, U.S.A. Carbonates Evaporites 20, 42–49. https://doi.org/10.1007/BF03175447.

Fletcher, R.C., Pollard, D.D., 1981. Anticrack model for pressure solution surfaces. Geology 9, 419–424. https://doi.org/10.1130/0091-7613(1981)9<419:AMFPSS>2.0.CO;2.

Gomez-Rivas, E., Martín-Martín, J.D., Bons, P.D., Koehn, D., Griera, A., Travé, A., Llorens, M.-G., Humphrey, E., Neilson, J., 2022. Stylolites and stylolite networks as primary controls on the geometry and distribution of carbonate diagenetic alterations. Mar. Petrol. Geol. 136, 105444 https://doi.org/10.1016/j.marpetgeo.2021.105444.

Gratier, J.-P., Favreau, P., Renard, F., Pili, E., 2002. Fluid pressure evolution during the earthquake cycle controlled by fluid flow and pressure solution crack sealing. Earth Planets Space 54, 1139–1146. https://doi.org/10.1186/BF03353315.

Gratier, J.P., Muquet, L., Hassani, R., Renard, F., 2005. Experimental microstylolites in quartz and modeled application to natural stylolitic structures. J. Struct. Geol. 27, 89–100. https://doi.org/10.1016/j.jsg.2004.05.007.

Greene, G.W., Kristiansen, K., Meyer, E.E., Boles, J.R., Israelachvili, J.N., 2009. Role of electrochemical reactions in pressure solution. Geochem. Cosmochim. Acta 73, 2862–2874. https://doi.org/10.1016/j.gca.2009.02.012.

Heald, M.T., 1959. Significance of stylolites in permeable sandstones. J. Sediment. Res. 29, 251–253. https://doi.org/10.1306/74D708F3-2B21-11D7-8648000102C1865D.

Heap, M.J., Baud, P., Reuschlé, T., Meredith, P.G., 2014. Stylolites in limestones: Barriers to fluid flow? Geology 42 (1), 51–54. https://doi.org/10.1130/G34900.

Hemelsdaël, R., Séranne, M., Husson, E., Ballas, G., 2021. Structural style of the Languedoc Pyrenean thrust belt in relation with the inherited Mesozoic structures and with the rifting of the Gulf of Lion margin, southern France. Bull. Soc. Geol. Fr. 192, 46. https://doi.org/10.1051/bsgf/2021037.

Hou, Z., Fusseis, F., Schöpfer, M., Grasemann, B., 2023. Synkinematic evolution of stylolite porosity. J. Struct. Geol. 173, 104916 https://doi.org/10.1016/j.jsg.2023.104916.

Hower, J., Eslin, E.V., Hower, M.E., Perry, E.A., 1976. Mechanism of burial metamorphism of argillaceous sediment: 1. Mineralogical and chemical evidence. GSA Bulletin 87, 725–737. https://doi.org/10.1130/0016-7606(1976)87<725:MOBMOA>2.0.CO;2.

Humphrey, E., Gomez-Rivas, E., Koehn, D., Bons, P.D., Neilson, J., Martín-Martín, J.D., Schoenherr, J., 2019. Stylolite-controlled diagenesis of a mudstone carbonate reservoir: A case study from the Zechstein_2_Carbonate (Central European Basin, NW Germany). Mar. Petrol. Geol. 109, 88–107. https://doi.org/10.1016/j.marpetgeo.2019.05.040.

Humphrey, E., Gomez-Rivas, E., Neilson, J., Martín-Martín, J.D., Healy, D., Yao, S., Bons, P.D., 2020. Quantitative analysis of stylolite networks in different platform carbonate facies. Mar. Petrol. Geol. 114, 104203 https://doi.org/10.1016/j.marpetgeo.2019.104203.

Katsman, R., 2010. Extensional veins induced by self-similar dissolution at stylolites: analytical modeling. Earth Planet Sci. Lett. 299, 33–41. https://doi.org/10.1016/j.epsl.2010.08.009.

Koehn, D., Rood, M.P., Beaudoin, N., Chung, P., Bons, P.D., Gomez-Rivas, E., 2016. A new stylolite classification scheme to estimate compaction and local permeability variations. Sediment. Geol. 346, 60–71. https://doi.org/10.1016/j.sedgeo.2016.10.007.

Laronne Ben-Itzhak, L., Aharonov, E., Karcz, Z., Kaduri, M., Toussaint, R., 2014. Sedimentary stylolite networks and connectivity in limestone: Large-scale field observations and implications for structure evolution. J. Struct. Geol. 63, 106–123. https://doi.org/10.1016/j.jsg.2014.02.010.

Lavenu, A.P.C., Lamarche, J., Salardon, R., Gallois, A., Marié, L., Gauthier, B.D.M., 2014. Relating background fractures to diagenesis and rock physical properties in a platform–slope transect. Example of the Maiella Mountain (central Italy). Mar. Petrol. Geol. 51, 2–19. https://doi.org/10.1016/j.marpetgeo.2013.11.012.

Maerten, L., Maerten, F., Lejri, M., Gillespie, P., 2016. Geomechanical paleostress inversion using fracture data. J. Struct. Geol. 89, 197–213. https://doi.org/10.1016/j.jsg.2016.06.007.

Mainprice, D., Hielscher, R., Schaeben, H., 2011. Calculating anisotropic physical properties from texture data using the MTEX open-source package. Geol. Soc., London, Spec. Publ. 360, 175–192. https://doi.org/10.1144/SP360.10.

Marshak, S., Engelder, T., 1985. Development of cleavage in limestones of a fold-thrust belt in eastern New York. J. Struct. Geol. 7, 345–359. https://doi.org/10.1016/0191-8141(85)90040-9.

Meng, Q., Hao, F., Tian, J., 2021. Origins of non-tectonic fractures in shale. Earth Sci. Rev. 222, 103825 https://doi.org/10.1016/j.earscirev.2021.103825.

Merino, E., Ortoleva, P., Strickholm, P., 1983. Generation of evenly-spaced pressure-solution seams during (late) diagenesis: A kinetic theory. Contrib. Mineral. Petrol. 82, 360–370. https://doi.org/10.1007/BF00399713.

Meunier, A., Velde, B., 1989. Solid solutions in I/S mixed-layer minerals and illite. Am. Mineral. 74, 1106–1112.

Meyer, E.E., Greene, G.W., Alcantar, N.A., Israelachvili, J.N., Boles, J.R., 2006. Experimental investigation of the dissolution of quartz by a muscovite mica surface: Implications for pressure solution. J. Geophys. Res. Solid Earth 111. https://doi.org/10.1029/2005JB004010.

Negrini, M., Smith, S.A.F., Scott, J.M., Tarling, M.S., 2018. Microstructural and rheological evolution of calcite mylonites during shear zone thinning: Constraints from the Mount Irene shear zone, Fiordland, New Zealand. J. Struct. Geol. 106, 86–102. https://doi.org/10.1016/j.jsg.2017.11.013.

Nelson, R.A., 1981. Significance of Fracture Sets Associated with Stylolite Zones1. AAPG (Am. Assoc. Pet. Geol.) Bull. 65, 2417–2425. https://doi.org/10.1306/03B599AE-16D1-11D7-8645000102C1865D.

Nenna, F., Aydin, A., 2011. The formation and growth of pressure solution seams in clastic rocks: A field and analytical study. J. Struct. Geol. 33, 633–643. https://doi.org/10.1016/j.jsg.2011.01.014.

Paganoni, M., Al Harthi, A., Morad, D., Morad, S., Ceriani, A., Mansurbeg, H., Al Suwaidi, A., Al-Aasm, I.S., Ehrenberg, S.N., Sirat, M., 2016. Impact of stylolitization on diagenesis of a Lower Cretaceous carbonate reservoir from a giant oilfield, Abu Dhabi, United Arab Emirates. Sediment. Geol. 335, 70–92. https://doi.org/10.1016/j.sedgeo.2016.02.004.

Park, W., Schot, E.H., 1968. Stylolitization in carbonate rocks. In: Recent Developments in Carbonate Sedimentology in Central Europe. Springer, pp. 66–74.

Peacock, D.C.P., Sanderson, D.J., 1995. Pull-aparts, shear fractures and pressure solution. Tectonophysics 241, 1–13. https://doi.org/10.1016/0040-1951(94)00184-B.

Petit, J.-P., Mattauer, M., 1995. Palaeostress superimposition deduced from mesoscale structures in limestone: the Matelles exposure, Languedoc, France. J. Struct. Geol. 17, 245–256. https://doi.org/10.1016/0191-8141(94)E0039-2.

Petit, J.-P., Wibberley, C.A.J., Ruiz, G., 1999. Crack–seal', slip: a new fault valve mechanism? J. Struct. Geol. 21, 1199–1207. https://doi.org/10.1016/S0191-8141(99)00038-3.

Philip, H., Bodeur, Y., Mattei, J., Mattauer, M., Therond, R., Paloc, H., Feraud, J., 1978. Notice de la carte géologique à 1/50 000, feuille Saint Martin de Londres.

Purcell, W.R., 1949. Capillary Pressures - Their Measurement Using Mercury and the Calculation of Permeability Therefrom. J. Petrol. Technol. 1, 39–48. https://doi.org/10.2118/949039-G.

Railsback, L.B., 1993. Lithologic controls on morphology of pressure-dissolution surfaces (stylolites and dissolution seams) in Paleozoic carbonate rocks from the mideastern United States. J. Sediment. Res. 63, 513–522. https://doi.org/10.2110/jsr.63.513.

Railsback, L.B., Andrews, L.M., 1995. Tectonic stylolites in the 'undeformed' Cumberland Plateau of southern Tennessee. J. Struct. Geol. 17, 911–915. https://doi.org/10.1016/0191-8141(94)00127-L.

Raynaud, S., Carrio-Schaffhauser, E., 1992. Rock matrix structures in a zone influenced by a stylolite. J. Struct. Geol. 14, 973–980. https://doi.org/10.1016/0191-8141(92)90028-U.

Renard, F., Dysthe, D., Feder, J., Bjørlykke, K., Jamtveit, B., 2001. Enhanced pressure solution creep rates induced by clay particles: Experimental evidence in salt aggregates. Geophys. Res. Lett. 28, 1295–1298. https://doi.org/10.1029/2000GL012394.

Renard, F., Gratier, J.-P., Jamtveit, B., 2000. Kinetics of crack-sealing, intergranular pressure solution, and compaction around active faults. J. Struct. Geol. 22, 1395–1407. https://doi.org/10.1016/S0191-8141(00)00064-X.

Renard, F., Ortoleva, P., Gratier, J.P., 1997. Pressure solution in sandstones: influence of clays and dependence on temperature and stress. Tectonophysics 280, 257–266. https://doi.org/10.1016/S0040-1951(97)00039-5.

Richard, J., Sizun, J.P., 2011. Pressure solution-fracturing interactions in weakly cohesive carbonate sediments and rocks: Example of the synsedimentary deformation of the Campanian chalk from the Mons Basin (Belgium). J. Struct. Geol. 33, 154–168. https://doi.org/10.1016/j.jsg.2010.11.006.

Rispoli, R., 1981. Stress fields about strike-slip faults inferred from stylolites and tension gashes. Tectonophysics 75, T29–T36. https://doi.org/10.1016/0040-1951(81)90274-2.

Rolland, A., Toussaint, R., Baud, P., Conil, N., Landrein, P., 2014. Morphological analysis of stylolites for paleostress estimation in limestones. Int. J. Rock Mech. Min. Sci. 67, 212–225. https://doi.org/10.1016/j.ijrmms.2013.08.021.

Rustichelli, A., Tondi, E., Agosta, F., Cilona, A., Giorgioni, M., 2012. Development and distribution of bed-parallel compaction bands and pressure solution seams in carbonates (Bolognano Formation, Majella Mountain, Italy). J. Struct. Geol. 37, 181–199. https://doi.org/10.1016/j.jsg.2012.01.007.

Séranne, M., Camus, H., Lucazeau, F., Barbarand, J., Quinif, Y., 2002. Polyphased uplift and erosion of the Cévennes (southern France). An example of slow morphogenesis. Bull. Soc. Geol. Fr. 173, 97–112. https://doi.org/10.2113/173.2.97.

Smith, J.V., 2000. Three-dimensional morphology and connectivity of stylolites hyperactivated during veining. J. Struct. Geol. 22, 59–64. https://doi.org/10.1016/S0191-8141(99)00138-8.

Soliva, R., Maerten, F., Petit, J.-P., Auzias, V., 2010. Field evidences for the role of static friction on fracture orientation in extensional relays along strike-slip faults: Comparison with photoelasticity and 3-D numerical modeling. Fault Zones 32, 1721–1731. https://doi.org/10.1016/j.jsg.2010.01.008.

Sorby, H.C., 1863. The Bakerian lecture: on the direct correlation of mechanical and chemical forces. Proc. Roy. Soc. Lond. 12, 538–550.

Stockdale, P.B., 1926. The Stratigraphic Significance of Solution in Rocks. J. Geol. 34, 399–414. https://doi.org/10.1086/623326.

Tada, R., Siever, R., 1989. Pressure solution during diagenesis. Annu. Rev. Earth Planet Sci. 17, 89.

Tavani, S., Storti, F., Lacombe, O., Corradetti, A., Muñoz, J.A., Mazzoli, S., 2015. A review of deformation pattern templates in foreland basin systems and fold-and-thrust belts: Implications for the state of stress in the frontal regions of thrust wedges. Earth Sci. Rev. 141, 82–104. https://doi.org/10.1016/j.earscirev.2014.11.013.

Tavani, S., Storti, F., Muñoz, J.A., 2010. Scaling relationships between stratabound pressure solution cleavage spacing and layer thickness in a folded carbonate multilayer of the Northern Apennines (Italy). J. Struct. Geol. 32, 278–287. https://doi.org/10.1016/j.jsg.2009.12.004.

Toussaint, R., Aharonov, E., Koehn, D., Gratier, J.-P., Ebner, M., Baud, P., Rolland, A., Renard, F., 2018. Stylolites: A review. J. Struct. Geol. 114, 163–195. https://doi.org/10.1016/j.jsg.2018.05.003.

Vandeginste, V., John, C.M., 2013. Diagenetic Implications of Stylolitization In Pelagic Carbonates, Canterbury Basin, Offshore New Zealand. J. Sediment. Res. 83, 226–240. https://doi.org/10.2110/jsr.2013.18.

Walderhaug, O., Oelkers, E.H., Bjørkum, P.A., 2004. An Analysis of the Roles of Stress, Temperature, and pH in Chemical Compaction of Sandstones: Discussion. J. Sediment. Res. 74, 447–449. https://doi.org/10.1306/092503740447.

Washburn, E.W., 1921. Note on a Method of Determining the Distribution of Pore Sizes in a Porous Material. Proc. Natl. Acad. Sci. USA 7, 115–116. https://doi.org/10.1073/pnas.7.4.115.

Willemse, E.J.M., Peacock, D.C.P., Aydin, A., 1997. Nucleation and growth of strike-slip faults in limestones from Somerset, U.K. J. Struct. Geol. 19, 1461–1477. https://doi.org/10.1016/S0191-8141(97)00056-4.

Yang, W., Zou, H., Li, T., Hu, L., Deng, C., Cheng, Z., Lan, C., Xu, Z., Chen, H., Lu, C., Li, P., 2022. Factors influencing stylolite formation in the Cambrian Longwangmiao Formation, Sichuan Basin, SW China. J. Petrol. Sci. Eng. 218, 110946 https://doi.org/10.1016/j.petrol.2022.110946.

Zhou, L., Wang, G., Hao, F., Xu, R., Jin, Z., Quan, L., Zou, H., 2022. The quantitative characterization of stylolites in the limestone reservoirs of the Lower Triassic Feixianguan Formation, northeastern Sichuan Basin: Insights to the influence of pressure solution on the quality of carbonate reservoirs. Mar. Petrol. Geol. 139, 105612 https://doi.org/10.1016/j.marpetgeo.2022.105612.

Zhou, X., Aydin, A., 2012. Mechanics of the formation of orthogonal sets of solution seams, and solution seams and veins and parallel solution seams and veins. Tectonophysics 532–535, 242–257. https://doi.org/10.1016/j.tecto.2012.02.013.